Scale dependence of earthquake rupture prestress in models with enhanced weakening: implications for event statistics and inferences of fault stress

Valere Lambert[1], Nadia Lapusta[1], and Daniel R. Faulkner[2]

[1]California Institute of Technology
[2]University of Liverpool

November 22, 2022

Abstract

Determining conditions for earthquake slip on faults is a key goal of fault mechanics highly relevant to seismic hazard. Previous studies have demonstrated that enhanced dynamic weakening (EDW) can lead to dynamic rupture of faults with much lower shear stress than required for rupture nucleation. We study the stress conditions before earthquake ruptures of different sizes that spontaneously evolve in numerical simulations of earthquake sequences on rate-and-state faults with EDW due to thermal pressurization of pore fluids. We find that average shear stress right before dynamic rupture (aka shear prestress) systematically varies with the rupture size. The smallest ruptures have prestress comparable to the local shear stress required for nucleation. Larger ruptures weaken the fault more, propagate over increasingly under-stressed areas due to dynamic stress concentration, and result in progressively lower average prestress over the entire rupture. The effect is more significant in fault models with more efficient EDW. We find that, as a result, fault models with more efficient weakening produce fewer small events and result in systematically lower b-values of the frequency-magnitude event distributions. The findings 1) illustrate that large earthquakes can occur on faults that appear not to be critically stressed compared to stresses required for slip nucleation; 2) highlight the importance of finite-fault modeling in relating the local friction behavior determined in the lab to the field scale; and 3) suggest that paucity of small events or seismic quiescence may be the observational indication of mature faults that operate under low shear stress due to EDW.

Scale dependence of earthquake rupture prestress in models with enhanced weakening: implications for event statistics and inferences of fault stress

Valère Lambert[1] Nadia Lapusta[1,2] Daniel Faulkner[3]

[1]Seismological Laboratory, California Institute of Technology, Pasadena, California, USA

[2]Department of Mechanical and Civil Engineering, California Institute of Technology, Pasadena, California, USA

[3]School of Environmental Sciences, University of Liverpool, Liverpool, UK

Key Points:

- Local shear prestress varies significantly within and among ruptures, being close to the quasi-static fault strength in nucleation regions.
- Efficient weakening allows rupture propagation over areas of lower prestress, leading to lower average prestress over larger rupture areas.
- Fault models with more efficient dynamic weakening produce fewer smaller events and result in systematically lower b-values.

Corresponding author: Valère Lambert, `vlambert@caltech.edu`

Abstract

Determining conditions for earthquake slip on faults is a key goal of fault mechanics highly relevant to seismic hazard. Previous studies have demonstrated that enhanced dynamic weakening (EDW) can lead to dynamic rupture of faults with much lower shear stress than required for rupture nucleation. We study the stress conditions before earthquake ruptures of different sizes that spontaneously evolve in numerical simulations of earthquake sequences on rate-and-state faults with EDW due to thermal pressurization of pore fluids. We find that average shear stress right before dynamic rupture (aka shear prestress) systematically varies with the rupture size. The smallest ruptures have prestress comparable to the local shear stress required for nucleation. Larger ruptures weaken the fault more, propagate over increasingly under-stressed areas due to dynamic stress concentration, and result in progressively lower average prestress over the entire rupture. The effect is more significant in fault models with more efficient EDW. We find that, as a result, fault models with more efficient weakening produce fewer small events and result in systematically lower b-values of the frequency-magnitude event distributions. The findings 1) illustrate that large earthquakes can occur on faults that appear not to be critically stressed compared to stresses required for slip nucleation; 2) highlight the importance of finite-fault modeling in relating the local friction behavior determined in the lab to the field scale; and 3) suggest that paucity of small events or seismic quiescence may be the observational indication of mature faults that operate under low shear stress due to EDW.

1 Introduction

Determining the absolute level and controlling factors of the stress state on faults has profound implications for earthquake physics, seismic hazard assessment, and the role of faulting in plate tectonics and geodynamics. Numerous lines of field evidence suggest that the average shear stress acting on mature faults must be low, 20 MPa or less, in comparison to the expected shear resistance of 100 - 200 MPa averaged over the seismogenic depth, given rock overburden and hydrostatic pore fluid pressure, along with typical quasi-static friction coefficients of 0.6 - 0.85 (aka "Byerlee friction") measured in laboratory experiments (Brune et al., 1969; Henyey & Wasserburg, 1971; Sibson, 1975; Byerlee, 1978; Lachenbruch & Sass, 1980; Townend & Zoback, 2004; Rice, 2006; Suppe, 2007; Tanikawa & Shimamoto, 2009; Nankali, 2011; Fulton et al., 2013; Gao & Wang, 2014). Such evidence includes the lack of a substantial heat flow anomaly around mature faults that would be expected for fault slip at 100 MPa or more (Brune et al., 1969; Henyey & Wasserburg, 1971; Lachenbruch & Sass, 1980; Nankali, 2011; Gao & Wang, 2014), inferences of steep angles between the principal stress direction and fault plane (Townend & Zoback, 2004), analyses of the fault core obtained by drilling through shallow parts of faults that have experienced major recent events, including the 2011 M_w 9.0 Tohoku-oki event (Tanikawa & Shimamoto, 2009; Fulton et al., 2013), the geometry of thrust-belt wedges (Suppe, 2007), and the existence of long-lived narrow shear zones that do not exhibit any evidence of melting (Sibson, 1975; Rice, 2006). Note that such evidence for apparent fault weakness pertains predominantly to mature faults, whereas some studies suggest that smaller, less mature faults may sustain the expected high shear stresses given Byerlee friction values and overburden minus hydrostatic pore pressure (e.g. Townend & Zoback, 2000).

A relatively straightforward explanation for the low-stress operation of mature faults is that they may be persistently weak (Figure 1), due to the presence of anomalously low quasi-static friction coefficients and/or low effective normal stress from pervasive fluid overpressure (Brown et al., 2003; Faulkner et al., 2006; Bangs et al., 2009; Collettini et al., 2009; Lockner et al., 2011). However, most materials with low quasi-static friction coefficients (less than 0.5) under laboratory conditions tend to exhibit velocity-strengthening behavior (Ikari et al., 2011), which would preclude spontaneous nucleation of dynamic ruptures. Moreover, while evidence of substantial fluid overpressure has been documented for many subduction zones (Brown et al., 2003; Bangs et al., 2009), there remains much debate over the ubiquity of chronic near-lithostatic fluid overpressurization along faults in other tectonic settings, such as continental faults, with some borehole measurements suggesting fluid pressure levels more consistent with hydrostatic conditions (Townend & Zoback, 2000; Zoback et al., 2010).

An alternative hypothesis for explaining such low-stress, low-heat operation is that mature faults are indeed strong at slow, quasi-static sliding rates but undergo considerable enhanced dynamic weakening at seismic slip rates, which has been widely hypothesized in theoretical studies and documented in laboratory experiments (Figure 1, dashed black line; Sibson, 1973; Tsutsumi & Shimamoto, 1997; Rice, 2006; Wibberley et al., 2008; Di Toro et al., 2011; Noda et al., 2009; Acosta et al., 2018). The presence of enhanced dynamic weakening on natural faults has been questioned by the expectation that enhanced dynamic weakening would produce much larger static stress drops than typical values of 1 to 10 MPa inferred from earthquakes on natural faults (Allmann & Shearer, 2009; Ye et al., 2016b). The expectation is based on a common assumption that the shear prestress over the entire rupture area should be near the static strength of the fault while the final shear stress should be near the dynamic strength of the fault, resulting in a large static stress change. However, a number of numerical and laboratory studies have demonstrated that, once nucleated, dynamic ruptures can propagate under regions with prestress conditions that are well below the expected static strength, based on prescribed or measured quasi-static friction coefficients and confining conditions (Zheng & Rice, 1998; Noda et al., 2009; Lu et al., 2010; Dunham et al., 2011; Gabriel et al., 2012; Fineberg & Bouchbinder, 2015) while the final shear stress could be higher then dynamic shear stress for pulse-like ruptures, with both inferences promoting reasonable stress drops. Such studies have often considered a single dynamic rupture nucleated artificially and propagating over uniform prestress conditions.

Recent numerical studies of earthquake sequences have shown that fault models with a combination of both hypotheses for low-stress operation, including some chronic fluid overpressure as well as mild-to-moderate enhanced dynamic weakening due to the thermal pressurization of pore fluids, work well for reproducing a range of observations (Perry et al., 2020; Lambert et al., in press). These include reasonable static stress drops between 1 - 10 MPa nearly independent of earthquake magnitude, the seismologically inferred increase in average breakdown energy with rupture size, the radiation ratios between 0.1 and 1 inferred for natural events, and the heat flow constraints. The simulations produce mainly crack-like or mild pulse-like ruptures, with no significant undershoot. The near magnitude-invariance of average static stress drop arises in these fault models because enhanced dynamic weakening results in both lower average prestress and lower average final shear stress for larger ruptures with larger slip, with the average static stress drops being nearly magnitude-independent. These studies suggest that distinguishing between the conditions required for rupture nucleation and propagation is important for assessing the relationship between laboratory friction measurements, seismological observations and the absolute stress conditions on faults.

Here, we use and expand upon the set of numerical models from Perry et al. (2020) and Lambert et al. (in press) to document the variability of prestress on a fault that arises from the history of previous ruptures, and to study the relation between the size of dynamic rupture events and the average shear prestress over the rupture area. We also examine how the complexity of earthquake sequences, in terms of the variability of rupture size, differs with the efficiency of dynamic weakening. We study these behaviors in the context of simulations of sequences of earthquakes and slow slip, which allow the prestress conditions before earthquakes to be set by the loading conditions, evolving fault shear resistance (including weakening and healing), and stress redistribution by prior slip, as would occur on natural faults. Moreover, our simulations resolve the spontaneous nucleation process with the natural acceleration of slow unsteady slip prior to dynamic rupture. The constitutive relations for the evolving fault resistance and healing adopted in our models have been formulated as a result of a large body of laboratory, field and theoretical work (e.g Sibson, 1973; Dieterich, 1979; Ruina, 1983; Rice, 2006; Wibberley et al., 2008; Di Toro et al., 2011). Indeed, laboratory experiments of fault shear resistance at both slow and fast slip rates have been indispensible for our understanding of fault behavior and for formulating fault models such as the ones used in this study. The modelling allows us to examine the implications of the laboratory-derived constitutive behaviors for the larger-scale behavior of faults, and we compare our inferences of average shear prestress from relatively large-scale finite-fault modeling to field measurements of crustal stresses acting on mature faults and small-scale laboratory measurements of the shear resistance of typical fault materials.

2 Building on laboratory constraints to model larger-scale fault behavior

Laboratory experiments have been instrumental for exploring aspects of fault resistance during both slow and fast sliding (10^{-9} m/s - 1 m/s, Figure 1). Experiments with slow sliding velocities ($< 10^{-3}$ m/s) are critical for formulating fault constitutive laws that form the basis for understanding the nucleation of earthquake ruptures. High-velocity laboratory friction experiments have demonstrated enhanced dynamic weakening of faults and elucidated a range of mechanisms by which this dynamic weakening can occur (e.g. Han et al., 2007; Wibberley et al., 2008; Goldsby & Tullis, 2011; Di Toro et al., 2011; Faulkner et al., 2011; De Paola et al., 2015; Acosta et al., 2018). Most slow- and high-velocity experiments measure or infer the relevant quantities - slip, slip rate, shear stress etc - averaged over the sample and examine the evolution of shear resistance corresponding to a particular history of loading, such as imposed variations in the displacement rate of the loading piston, and the particular fault conditions (normal stress, temperature, pore fluid pressure, etc.). Some experimental studies imposed the expected sliding motion during earthquakes in order to directly relate laboratory stress measurements to seismological quantities, such as static stress drop and breakdown energy (e.g. Sone & Shimamoto, 2009; Fukuyama & Mizoguchi, 2010; Nielsen et al., 2016).

To understand the full implications of the evolution of shear resistance measured in small-scale experiments for slip at larger scales along natural faults, they are synthesized into mathematical formulations and used in numerical modeling, for the following reasons. During slipping events on a finite fault over scales of tens of meters to kilometres - much larger than the experimental scale - the fault does not slip uniformly with a predetermined slip-rate history. Rather, the slip event initiates on a portion of the fault and then spreads along the fault, with varying slip-rate histories and final slips at different points along the fault. This is captured in inversions of large earthquakes (e.g. Heaton, 1990; Simons et al., 2011; Ye et al., 2016a; Tinti et al., 2016) and, to a degree, in larger-scale experiments, sometimes involving analog materials (Lu et al., 2010; McLaskey et al., 2014; Svetlizky & Fineberg, 2014; Yamashita et al., 2015; Rubino et al., 2017). In the process, the slip (1) transfers stress to the more locked portions of the fault and (2) enters portions of the fault with different conditions - such as levels of shear pre-stress, pore fluid pressure, etc - and potentially different friction and hydraulic properties. Hence the resulting coupled evolution of shear resistance and slip rate at different locations on the fault is often quite different and, through stress transfer, strongly dependent on the entire slip process at all locations throughout the rupture. These nonlinear and often dynamic feedback processes on the scales of tens of meters to kilometers can currently be only captured through numerical modeling.

Many numerical models of earthquake source processes utilize insight from laboratory experiments that indicate that the resistance to shear τ along a fault depends on the sliding rate V and the quality and/or lifetime of the local contacts, typically parameterized by a state variable θ with units of time, as well as on the effective normal stress $\overline{\sigma} = \sigma - p$ acting on the fault, with σ being the normal stress and p being the pore fluid pressure localized within the shearing layer (e.g. Dieterich, 1979; Marone, 1998). For continuum problems involving frictional sliding, the motion within the continuum is governed by the balance of linear momentum, subject to the boundary condition that tractions are given by the constitutive law of the interface. For frictional sliding without changes in the elastodynamic normal stress, which is the case considered in this work, the boundary condition reduces to the shear stress being equal to the shear resistance on the interface ($y = 0$):

$$\begin{aligned} \tau_{\text{stress}}(x, y = 0, z; t) &= \tau_{\text{resistance}}(x, y = 0, z; t) \\ &= f(V, \theta)(\sigma - p). \end{aligned} \tag{1}$$

An important concept in the rate-and-state formulation of the friction coefficient $f(V, \theta)$ is that the friction coefficient is not a fixed property of the interface but evolves over time, facilitating the time-dependent changes of shear resistance and hence shear stress along the fault during shear.

The most commonly used formulation of rate-and-state laws is the Dieterich-Ruina formulation (Dieterich, 1979; Ruina, 1983):

$$f(V, \theta) = \left[f_* + a \ln \frac{V}{V_*} + b \ln \frac{\theta V_*}{L} \right], \tag{2}$$

where f_* is a reference steady-state friction coefficient at the reference sliding rate V_*, L is the characteristic slip distance, and a and b are the direct effect and evolution effect parameters, respectively. Our fault models are governed by a form of the laboratory-derived Dieterich-Ruina rate-and-state friction law regularized for zero and negative slip rates (Lapusta et al., 2000; Noda & Lapusta, 2010). The evolution of the state variable can be described by various evolution laws; we employ the aging law (Ruina, 1983):

$$\dot{\theta} = 1 - \frac{V\theta}{L}, \tag{3}$$

which describes evolution during sliding as well as time-dependent healing in near-stationary contact. In our models, the shear resistance and shear stress also change due to the evolution of pore fluid pressure p.

We conduct numerical simulations following the methodological developments of Lapusta et al. (2000), Noda and Lapusta (2010) and Lambert et al. (in press) in order to solve the elastodynamic equations of motion with the fault boundary conditions, including the evolution of pore fluid pressure and temperature on the fault coupled with off-fault diffusion. The simulations solve for mode III slip on a 1-D fault embedded into a 2-D uniform, isotropic, elastic medium (Figure 2). The potential types of slip on the fault include sequences of earthquakes and aseismic slip (SEAS) and they are simulated in their entirety, including the nucleation process, dynamic rupture propagation, post-seismic slip that follows the event, and interseismic period between seismic events that can last up to tens or hundreds of years and host steady and transient slow slip (Figure 2).

The simulated fault in our models contains a 24-km-long segment with velocity-weakening (VW) frictional properties where earthquake ruptures may nucleate and propagate, surrounded by velocity-strengthening (VS) segments that inhibit rupture nucleation and propagation. Our simulations include enhanced dynamic weakening due to the thermal pressurization of pore fluids, which occurs when pore fluids within the fault shearing layer heat up and pressurize during dynamic rupture, reducing the effective normal stress and shear resistance (Sibson, 1973; Rice, 2006; Noda & Lapusta, 2010). Thermal pressurization is one potential mechanism for enhanced weakening; qualitatively similar results should hold for models with other types of enhanced dynamic weakening. We follow the thermal pressurization formulation of Noda and Lapusta (2010) (Supplementary Materials).

For the purpose of comparing local frictional behavior with the average prestress for dynamic ruptures of varying sizes, we focus this study on simulated ruptures that arrest within the VW region, where the friction properties are uniform with a quasi-static reference friction of 0.6, consistent with many materials exhibiting VW behavior in laboratory experiments (Ikari et al., 2011). We examine the evolution of the apparent friction coefficient, or the ratio of the current shear stress τ to the interseismic drained effective normal stress $(\sigma - p_{\text{int}})$, where p_{int} is the interseismic drained value of the pore pressure. The "drained" refers to the effective stress with ambient pore pressure unaffected by slip processes such as dilatancy, compaction, or thermal pressurization.

We examine fault models with varying levels of ambient fluid overpressure in terms of the effective normal stress, as well as varying degrees of efficiency in enhanced weakening due to thermal pressurization. The parameter values we have chosen (Tables 1-3) are motivated by prior studies that have reproduced a range of seismological observations as well as low-stress, low-heat operation of mature faults (Perry et al., 2020; Lambert et al., in press). The parameter values also facilitate our goal of examining ruptures in fault models with a range of efficiency in enhanced dynamic weakening. We define the beginning and end of dynamic rupture, t_{ini} and t_{fin} respectively, as well as the ruptured area Ω, using a slip velocity threshold ($V_{\text{thresh}} = 0.01$ m/s) for seismic slip, based on previous studies (Perry et al., 2020; Lambert et al., in press). Note that t_{ini} and t_{fin} refer to the beginning and end of the entire rupture event, which starts when one location on the fault reaches the threshold velocity and ends when all points on the fault drop below the threshold velocity. In the following, we use "rupture" to refer to such dynamic slip events, unless noted otherwise. Further description of the numerical methodology can be found in the Supplementary Materials.

3 Evolution of local slip and shear resistance and notions of failure

Our simulations capture the evolution of motion and shear stress across the fault over sequences of earthquakes spanning several thousands of years (Figure 2C). The initial distributions of shear stress and other quantities such as the slip rate are assumed to be uniform along most of the VW region of the fault at the start of our simulations, other than a small region of initially high prestress near the VW-VS boundary to nucleate the first rupture in the earthquake sequence. The distributions of shear stress and slip along the fault evolve to become highly variable throughout periods of fast earthquake-producing slip as well as slow aseismic slip and fault locking. Below we review how the rate-and-state friction framework allows the model to represent both creeping, locked, and seismically slipping fault areas as well as transitions between these different styles of slip.

During dynamic rupture, the evolution of slip rate and shear stress can be particularly complex and variable along the fault. At points where individual ruptures nucleate, the slip rate gradually accelerates towards seismic slip rates and shear stress at the beginning of rupture, t_{ini}, is relatively high, with the apparent friction coefficient $\tau/(\sigma - p_{\mathrm{int}})$ close to the quasi-static reference friction of 0.6. As seismic slip rates are reached, $\tau/(\sigma - p_{\mathrm{int}})$ drops substantially due to thermal pressurization of pore fluids in a manner qualitatively consistent with the enhanced dynamic weakening observed in high-velocity laboratory friction experiments (Figure 2H). The evolution of slip rate and shear stress outside of the nucleation region is even more complicated: The shear stress at t_{ini}, prior to the arrival of the rupture front, can be much lower than the shear stress levels where the rupture nucleates, then increases to a higher peak shear stress that reflects the interseismic fault healing and rate-and-state direct effect and is achieved due to the dynamic stress concentration at the rupture front, and then decreases due to weakening with seismic slip (Figure 2H vs. I). Consistently, the slip rate rapidly increases to seismic values at the beginning of slip and then decreases, as in a typical Yoffe-like behavior for dynamic ruptures (Figure 2G; e.g Tinti et al., 2005). Thus, even with the uniform normal stress and uniform parameters of the assumed friction and pore pressure equations within the seismogenic VW region, the prestress conditions throughout the rupture area can be highly variable and, in part, substantially different between regions of rupture nucleation and rupture propagation.

Note that the peak shear stress during dynamic rupture of fault locations outside the nucleation zone can correspond to much higher apparent friction coefficient (e.g., 0.95 in Figure 2I) than the reference friction coefficient ($f_* = 0.6$ in this study). This is due to both the direct effect at the rupture tip and the high, interseismically "healed" value of the state variable θ, as discussed in Lambert and Lapusta (2020) and the Supplementary Materials (equation S3). As follows from the first line of equation S3, the difference between the peak friction coefficient and f_* due to the direct effect of $a \ln(V_{\text{peak}}/V_*)$ would be 0.14 to 0.16 for $V_{\text{peak}} = 1$ to 10 m/s and other parameters of our model, with the rest due to the much larger value of the "healed" state variable than that for sliding at the reference sliding rate.

The local evolution of shear stress throughout the VW seismogenic zone differs among points based on the long-term history of motion, including both local slip as well as slip across the entire fault. For example, a point at the center of the VW region (z = 0 km) of one of our simulations (fault model TP 3 in Table 2, as shown in Figure 2C) experiences substantial slip only during the largest earthquake ruptures that span the entire VW domain, resulting in a relatively simple and quasi-repetitive pattern of stress accumulation and weakening over sequences of earthquakes (Figure 3A & C). In contrast, another point in the VW region closer to the VS boundary (z = -9.6 km) experiences different amounts of slip during dynamic ruptures of varying size, resulting in a more complicated evolution of shear stress with accumulating slip (Figure 3B & D).

In between individual earthquakes, the VS regions of the fault creep (i.e., slowly slip) with the slip rate close to the prescribed tectonic plate rate, due to that rate being imposed on the fault areas nearby, with occasional quasi-static accelerations due to post-seismic slip (Figure 4, left column). The creep penetrates into the VW regions nearby, creating fault areas prone to earthquake nucleation (Jiang & Lapusta, 2016; Michel et al., 2017) (Figure 4, right column). These points of the VW region close to the VS region (within one or so nucleation length) are reloaded due to creep and post-seismic slip from previous rupture within the VS regions. The loading rate at these points near the VS-VW boundary varies over time depending on the rate of motion in the VS region, which in turn depends on the previous history of co-seismic slip during dynamic ruptures in the VW region.

The slip rate and apparent friction at points close to the VW-VS boundary are typically brought to near steady conditions around the loading plate rate, however both exhibit small oscillations as these points continue to be loaded by creep in the VS region, resulting in further acceleration, slip and weakening, and thus the transmission of stress further into the VW region until a sufficiently large area is loaded to sustain rupture nucleation and acceleration to seismic slip rates (Figure 4E-G). This oscillatory behavior is consistent with predictions from the stability analysis of a single degree-of-freedom spring-slider undergoing frictional slip, where the amplitude of the oscillations is expected to grow as the spring stiffness decreases below a critical stiffness value until (Gu et al., 1984). The effective stiffness of the slipping fault zone in a continuum model is inversely proportional to the slipping zone side (Rice & Ruina, 1983), decreasing with the increasing slipping region. Note that this rate-and-state nucleation process has been used to explain the period-dependent response of microseismicity to periodic stress perturbations in Nepal, where seismicity shows significant variations in response to annual monsoon-induced stress variations but not to semidiurnal tidal stresses of the same magnitude (Ader et al., 2014).

In contrast, much of the VW region further away from the VS regions is essentially locked, which is expressed in the rate-and-state formulation as sliding at very low, but still non-zero, slip rates that are many orders of magnitude smaller than the loading rate (Figure 5A-B). This differential motion between the VS and VW regions loads points in the VW region (Figure 5C-D), gradually increasing shear stress there (e.g., between 700 and 800 years in Figure 5C). Note that the interseismic stressing rate is higher at locations closer to the creeping regions than further away from it (Figures 5C vs. 5D vs.

4F), as one would expect. At the same time, the essentially locked points within the VW region experience time-dependent healing of the local shear resistance encapsulated in the increase of the state variable θ (Figure 5E-F). One of the manifestations of this healing is that larger interseismic increases in the state variable generally lead to higher peak shear stress during dynamic rupture propagation (Lambert & Lapusta, 2020). Despite the increase in the state variable, its value is far below the steady-state one for the very low interseismic slip rates, consistent with continuing healing prior to dynamic rupture (Figure 5G-H). Depending on whether the local shear stressing rate (which increases the shear stress τ on the left of equation 1) is larger or smaller than the rate of healing (expressed by the last, θ term on the right hand side of equation 2), the local slip rate (that enters the second term of equation 2) increases (as between 700 and 800 years in Figure 5A) or decreases, i.e., the fault is accelerating towards failure or becomes even more locked. However, most of the locked points of the fault never accelerate close to failure interseismically; rather, they fail due to stress concentrations from dynamic events, seen as vertical lines in Figure 5C-D.

We note that healing on natural faults, in the presence of fluids and depth-dependent elevated temperatures, can be affected by a number of mechanisms that are not captured by the basic state evolution equation (Yasuhara et al., 2005; Tenthorey & Cox, 2006; Chen et al., 2015a, 2015b). Incorporating more realistic healing into shear resistance formulations and numerical modelling is an important goal for future work. This can be done by modifying the evolution of the state variable θ or adding other state variables that would encode healing. Yet, qualitatively, additional healing mechanisms would have similar effects on the simulations as the current rate-and-state healing, in that the healing would modify the peak shear resistance and the subsequent evolution of the resistance based on the interseismic fault state, potentially further amplifying differences in shear resistance evolution for different points along the fault (e.g., nucleation points vs. locked points) that our simulations already highlight.

The presence of time-dependent healing as well as persistent, potentially unperceivable, slow (quasi-static) motion and its acceleration under variable levels of shear stress illustrate how the concepts of failure, and hence strength, are not easily defined for frictional sliding. For realistic frictional interfaces, the precise value of a static friction coefficient is ill-defined, since no interface loaded in shear is perfectly static; rather creep processes occur at slow, unperceivable slip rates at any level of shear loading (Dieterich & Kilgore, 1994; Bhattacharya et al., 2017) and/or over parts of the contacting interfaces (Rubinstein et al., 2004, 2006; Ben-David et al., 2010). Hence the transition from locked interfaces to detectable slip is always a gradual process (although it may be occurring faster than the time scales of interest/observation in many applications). This reality is reflected in lab-derived fault constitutive relations such as rate-and-state friction. Since failure typically refers to the presence of irreversible or inelastic deformation, frictional interfaces may be considered failing under any style or rate of motion, be it during slow steady sliding, transient slow slip, or dynamic rupture. Therefore, any meaningful notion of strength first requires definition of the failure of interest, e.g., reaching seismic slip rates of the order of 1 m/s. Without such explicit definition, failure is then implicitly defined as transition from locked to slipping and corresponds to sliding with a detectable velocity; for laboratory experiments or observational studies, this would imply that whether the interface is locked or slipping depends on the instrumental precision for detectable motion.

In this study, we would like to compare the shear stress values required for aseismic slip nucleation and for dynamic rupture propagation. During spontaneous aseismic slip nucleation, the slip rates evolve from very low to seismic, passing in the process through the slip rate equal to the tectonic loading rate V_{pl}. In the standard rate-and-state friction, at each fixed sliding rate V, the friction coefficient eventually evolves to a steady-state value $f_{ss}(V)$ (equation S2; for very small slip rates, the regularized formulation of equation S5 needs to be considered). Under slow loading, aseismic earthquake nucleation on a finite fault is typically a gradual process, with many points within the nucleation zone being close to the steady state (Figure 4; Rubin & Ampuero, 2005; Kaneko & Lapusta, 2008). While the steady-state values of friction depend on the sliding rate, the dependence is relatively minor at the low, quasi-static slip rates between the plate rate of approximately 10^{-9} m/s and sub-seismic slip rates of $< 10^{-3}$ m/s (Figure 1) which are relevant for fault creep and earthquake nucleation, and for which the standard rate-and-state formulation is (approximately) valid. The product of this collection of steady-state quasi-static friction coefficients and the interseismic drained effective stress gives the shear resistance of faults at sustained slow sliding rates, which we call the *steady-state quasi-static fault shear resistance* (referred to in short as local SSQS shear resistance). As the representative value of such local SSQS shear resistance, we choose the shear resistance of the fault steadily creeping at the prescribed long-term tectonic plate rate V_{pl} (which the fault would have long-term if it were slipping stably), with the interseismic drained value of the pore pressure p_{int}:

$$\tau_{ss}^{V_{\mathrm{pl}}}(z,t) = (\sigma - p_{\mathrm{int}})\, f_{ss}(V_{\mathrm{pl}}) \tag{4}$$

In our models, $\tau_{ss}^{V_{\mathrm{pl}}} / (\sigma - p_{\mathrm{int}}) = 0.63$ within the VW region. Note that choosing V_* instead of V_{pl} would result in a similar value of $\tau_{ss}^{V_{\mathrm{pl}}} / (\sigma - p_{\mathrm{int}}) = f_* = 0.6$.

In the following section, we compare this representative value of local SSQS shear resistance to the spatial distribution of shear stress prior to dynamic ruptures in our simulations. Note that the local SSQS shear resistance is similar to what is typically viewed as "frictional fault strength" in the sense of Byerlee (1978), i.e., this is the resistance that needs to be met for noticeable quasi-static slip with the loading rate or another reference rate.

4 Larger ruptures associated with lower shear prestress over the rupture scale but higher prestress over smaller scales near nucleation

The interseismic periods in between individual earthquake ruptures in our simulations vary from months to decades, depending on the size of the rupture and the stress state resulting from the history of prior slip along the fault. Our earthquake sequence simulations produce a wide variety of rupture sizes due to heterogeneous prestress conditions along the fault that spontaneously arise in our models.

Let us consider the evolution of slip and shear stress in representative simulated spontaneous ruptures of increasing sizes within the same simulation (Figure 6). Over sequences of rupture events, the shear stress conditions prior to and after individual dynamic ruptures become spatially heterogeneous. This stress heterogeneity is due in part to the history of spatially variable slip and local static stress drop produced in previous ruptures, as well as stress relaxation and redistribution due to aseismic slip. In addition, while our simulated fault models are loaded by a constant long-term loading rate of V_{pl}, the effective loading conditions along the fault interface vary in space and time due to differences in slip rate along the fault. Ruptures nucleate preferentially in regions with the highest shear prestress, which in our models occur near the creeping regions as discussed in section 3 (Figure 6). The ruptures then propagate into the less stressed areas of the fault. Put another way, the average prestress over the nucleation region is higher than the average prestress over the entire ruptured region (Figure 7A vs. B), as we quantify in the following.

We compute the average shear prestress right before a dynamic rupture event over the entire future rupture area (which we do as post-processing of data in our simulation). We also compute the average shear prestress over the slow-slip nucleation zone, which we call the *nucleation stress*. We compare these average shear stress measures with the *local steady-state quasi-static (SSQS) fault shear resistance* $\tau_{ss}^{V_{\mathrm{pl}}}$, which is related to the local fault constitutive properties during slow slip and given by equation 4.

Averaging of spatially variable stress fields can be done in several different ways (Noda & Lapusta, 2012; Noda et al., 2013). The simplest definition of the average shear prestress over the rupture region Ω is the spatially averaged prestress τ^A_{ini} acting in the overall slip direction at the beginning of the rupture t_{ini}, given by:

$$\tau^A_{\text{ini}} = \frac{\int_\Omega \tau(z, t_{\text{ini}})dz}{\int_\Omega dz}. \tag{5}$$

We can similarly define the spatially averaged nucleation stress τ^A_{nucl} within the nucleation region. We define the nucleation region to be the fault segment between the expanding stress fronts at the initiation of dynamic rupture; the size of the nucleation regions in our simulations is comparable to the theoretical nucleation size estimate h^*_{RA} of Rubin and Ampuero (2005) (equation S6, Figure S1).

Not surprisingly and consistent with prior studies, we find that the spatially averaged nucleation stress τ^A_{nucl} for our simulated ruptures is comparable to the local SSQS shear resistance $\tau_{ss}^{V_{\text{pl}}}$ (Figure 7A). As a consequence, it does not significantly depend on the ultimate rupture size or slip. Since the nucleation stress here is computed at the beginning of dynamic rupture, it is then the shear stress within the nucleation zone at the end of the nucleation, when parts of the zone slip with near-dynamic slip rates approaching 10^{-2} m/s. That is why the nucleation stress is systematically slightly lower than the local SSQS shear resistance defined as the steady-state shear resistance to slip with the (lower) plate rate. The difference between the nucleation stress and local SSQS shear resistance could be more substantial if dynamic weakening were efficient enough to affect some portion of the earthquake nucleation region (Segall & Rice, 2006).

In contrast, the spatially averaged prestress over the entire ruptured area τ^A_{ini} tends to decrease with the rupture size and increasingly deviate from the local SSQS shear resistance and nucleation stress for increasingly efficient dynamic weakening (Figures 6 & 7B). Such behavior is also true for another average prestress measure, the energy-based average prestress $\overline{\tau}^E_{\text{ini}}$ (Noda & Lapusta, 2012), which is the average shear prestress weighted by the final slip of the rupture, and hence represents the average prestress associated with the potency of the impending rupture:

$$\overline{\tau}^E_{\text{ini}} = \frac{\int_\Omega \tau(z, t_{\text{ini}})\delta_{\text{fin}}(z)dz}{\int_\Omega \delta_{\text{fin}}(z)dz} \tag{6}$$

where $\delta_{\text{fin}}(z) = \delta(z, t_{\text{fin}}) - \delta(z, t_{\text{ini}})$ is the final local slip accrued in the rupture. We denote $\overline{\tau}^E$ with a bar as it not only represents an average over space but also requires knowledge of the final slip of the rupture. $\overline{\tau}^E_{\text{ini}}$ differs from the spatially-averaged prestress τ^A_{ini} over the rupture area when the resulting slip distribution is not uniform. We find that $\overline{\tau}^E_{\text{ini}}$ and τ^A_{ini} for our simulated ruptures are comparable and vary similarly with the rupture size and efficiency of dynamic weakening, with the values of $\overline{\tau}^E_{\text{ini}}$ being slightly larger (Figure S2).

The finding that larger ruptures are associated with smaller average shear prestress over the ruptured area may appear counterintuitive. Why do smaller ruptures not become larger if they are more favorably prestressed? To understand this behavior, let us consider the prestress averaged over several fixed scales around the nucleation region for ruptures of different sizes. We locate the VW-VS boundary next to which each of our simulated ruptures nucleate and average the prestress along the VW region over fixed distances (1, 2, 4, 8, 12 and 16 km) from the corresponding VW-VS boundary (Figure 8; shown for fault model TP4 from Table 2). While the spatially-averaged prestress over the entire rupture length decreases with increasing rupture size, we see that the prestress spatially-averaged over smaller fixed scales is generally higher for larger ruptures than for smaller ruptures (Figure 8 warmer vs cooler colored triangles). For smaller ruptures, the average shear stress over scales just larger than their total rupture length is lower than the average prestress of larger ruptures with comparable length to the fixed averaging scales (Figure 8, triangles below the circles). This confirms that the smaller ruptures arrest because the prestress conditions ahead of the rupture are too low to sustain further rupture propagation. For larger ruptures, the average prestress levels at scales smaller than their total rupture length are generally higher or comparable to the average prestress over smaller ruptures with the length comparable to the fixed averaging scales (Figure 8, triangles above the circles). This finding suggests that larger ruptures have higher, more favorable average prestress conditions at smaller scales compared to smaller ruptures, which facilitates continued rupture propagation. Hence we find that the shear prestress prior to our simulated ruptures of varying sizes self-organizes into a spatial distribution of scale-dependent average shear stress that governs the rupture occurrence.

5 Role of dynamic stress transfers and motion-dependent local shear resistance

Such scale- and motion-dependent average fault shear prestress before ruptures results from two related and interacting factors. First, as dynamic rupture propagates, some of the released energy is carried by waves along the fault, creating a substantial stress concentration near the rupture tip that is a well-known feature of dynamic rupture (e.g., Freund, 1990). The stress concentration enables rupture propagation over regions where the prestress is lower than the local SSQS shear resistance, drawing the local shear stress up to the peak stress before the subsequent stress drop due to local weakening (black lines in Figure 6). The dynamic stress concentration increases with the rupture dimension and/or slip and thus allows larger ruptures to continue propagating over regions with lower, and hence less favorable, prestress conditions (Figure 6). This is illustrated in this work for largely crack-like ruptures that occur in the presented models with mild to moderate enhanced dynamic weakening (Lambert et al., in press), but similar conclusions would be reached for pulse-like ruptures provided that they satisfy the observational constraint of magnitude-independent stress drops, which implies that ruptures with larger magnitudes would have larger average slip and hence larger stress concentrations. Note that a pulse-like rupture with the same or similar spatial distribution of the slip rate (and hence the same local slip) propagating along the fault would result in a similar stress concentration at the rupture tip regardless of the rupture length; however, in that scenario, pulses with larger rupture propagation lengths would have systematically lower static stress drops, as the stress drops would be proportional to the (uniform) pulse slip divided by ever increasing propagation lengths.

Second, the evolving local shear resistance substantially depends on both the prior history of slip events on the fault through fault prestress and on the motion during the current rupture event through dynamic stress transfers that add substantial time-dependent loading. This pronounced dependence is due to strong coupling between the evolving motion, the resulting shear heating, and the evolving shear resistance. As a result, the evolution of local slip rate and local shear resistance (1) significantly differs at different fault locations of each rupture (despite uniform constitutive properties) and (2) significantly differs at the same fault location for different ruptures (Figures 2D-I and 6D-E).

These two factors create a substantial positive feedback, in which larger ruptures with more slip generate larger stress concentrations, leading to faster and larger slip, which dynamically causes more fault weakening, which in turn promotes more/faster slip, more energy release, larger stress concentrations, and increasing rupture sizes.

The result that larger ruptures are associated with lower average prestress indicates the need for increasingly less favorable stress conditions to arrest growing ruptures. For a given rupture size, if the prestress ahead of the rupture is favorable, then the rupture would continue to grow until it experiences sufficiently unfavorable prestress conditions, thus lowering the overall average prestress. Alternatively, the rupture may be forcibly arrested by other means such as strong geometric or rheological barriers. For example, ruptures propagating over higher prestress conditions within the VW region can be arrested by fault regions with VS properties; in those cases, the overall average prestress conditions would depend on the properties of the VS regions (Perry et al., 2020). Detailed study of the implications of fault geometry and heterogeneity for rupture arrest and the average stress conditions prior to rupture is an important topic for future work.

6 Comparison of finite-fault modeling to single-degree-of-freedom representations

As captured in field observations of natural earthquakes and reflected in our simulations, sufficiently large earthquake ruptures nucleate on a subsection of the fault and then propagate through other sections of the fault. Capturing such space-dependent behavior is typically called "finite-fault" modeling, in contrast to the point source that considers a spatially average representation of an event, as if it occurs at one "point". A typical numerical model of a point source is the single-degree-of-freedom system (SDOF) of a slider with friction pulled by a spring (e.g. Dieterich, 1979; Ruina, 1983; Rice & Ruina, 1983). Small-scale laboratory experiments often measure properties averaged over a sample and are typically modeled as a SDOF spring-slider systems.

The significant role of spatially varying prestress conditions and dynamic stress transfers during rupture propagation in determining the rupture behavior implies that capturing the finite-fault nature of the process is essential for determining the stress evolution characteristic of dynamic rupture. For example, several laboratory studies applied variable slip rates histories inferred from natural earthquakes to rock samples, measured the resulting shear resistance, and then related laboratory stress measurements to seismological source properties such as breakdown energy and stress drops (e.g. Sone & Shimamoto, 2009; Fukuyama & Mizoguchi, 2010; Nielsen et al., 2016). Such experiments have provided invaluable data about the local shear resistance of faults, specifically enhanced dynamic weakening, that have informed theoretical and numerical modeling of finite faults (e.g. Zheng & Rice, 1998; Rice, 2006; Noda et al., 2009; Noda & Lapusta, 2010; Dunham et al., 2011; Gabriel et al., 2012; Perry et al., 2020; Lambert et al., in press), including the current study. However, the interpretation of such experiments needs to take into account their SDOF nature. For example, to improve alignment etc, the experiments often impose pre-sliding at slow slip rates (of the order of micron/s) prior to imitating seismic motion. That procedure results in the shear prestress before seismic slip comparable to the local SSQS shear resistance (equation 4) and near steady-state values of the state variable, as appropriate for a location within a nucleation zone. In contrast, our simulations show that most points on a fault through which the rupture propagates have much lower shear prestress and much larger values of the state variable corresponding to well-healed fault (Figures 6 and 9B). Furthermore, the experiments often apply smoothened slip-rate histories obtained from finite-fault inversions, while the stress concentration at the tip of dynamic rupture makes the slip rate variation much more dramatic.

To illustrate the differences for the shear resistance evolution obtained with such experimental procedures versus the one from our simulated finite-fault models, let us compare the local fault behavior during one of our dynamic ruptures with a SDOF calculation. In the SDOF calculation, we use the same fault properties (equations 3, S4 and S7-8) and same parameter values as in the finite-fault VW regions but apply quasi-static presliding and modified, smoothened slip rates motivated by the laboratory procedures of Fukuyama and Mizoguchi (2010) (further details in Supplementary Materials). We conduct the comparison for two fault locations, one in the nucleation region and one within dynamic rupture propagation region (Figure 9). These SDOF calculations are successful at reproducing the presence of the enhanced dynamic weakening with slip as occurs during dynamic ruptures and generally capture the more moderate slip evolution and behavior of points within the nucleation region of our simulated dynamic ruptures. At the same time, the overall shear stress evolution during typical propagation of the dynamic rupture substantially differs from that of the SDOF calculation, with notable features including the low initial stress (which depends on prior slip history) relative to the SSQS shear resistance, the much more dramatic increase in shear stress associated with the dynamic rupture front (which arises due to the more healed fault coupled with the dynamic stress concentration), and the shear stress evolution at the end of slip (which depends on the final slip distribution over the entire finite fault) (Figure 9).

7 Implications for earthquake statistics

A notable feature of the scale dependence of average prestress before dynamic rupture is that, as an earthquake grows larger, the prestress needed for further propagation decreases (Figure 7B). In addition, the higher the weakening rate, the easier it should be for a rupture to have favorable prestress conditions to continue growing, rather than arresting as a smaller earthquake. Hence one could hypothesize that the more efficient the enhanced dynamic weakening, the smaller the complexity of the resulting earthquake sequences, with increasing representation of larger events at the expense of smaller events.

This is exactly what our modeling shows (Figure 10). The fault models with increasingly more efficient weakening produce earthquake sequences with increasingly fewer small events and decreasing b-values of the cumulative size distribution (Figure 10). Fault models with even more efficient dynamic weakening than considered in this study, such as those that produce sharp self-healing pulses, result in relatively simple earthquake sequences consisting of only large events (Lambert et al., in press). The fault models governed by relatively mild to more moderate weakening as considered in this work develop a wider range of earthquake sizes, due to a feedback loop of more likely rupture arrest due to milder weakening creating stress heterogeneity that in turn makes rupture arrest more likely. This result is consistent with those of previous quasi-dynamic earthquake sequence simulations demonstrating complex earthquake sequences with b-values around 0.75 on faults with standard rate-and-state friction only and milder quasi-dynamic stress transfer (Cattania, 2019). Our study shows that the b-values decrease to 0.5 for fully dynamic simulations without enhanced dynamic weakening, and further decrease to 0.25 or so for the most efficient weakening considered in this study.

While the frequency-magnitude distribution of seismicity over relatively large regions, such as Northern or Southern California, is generally well-described by Gutenberg-Richter scaling with typical b-values near unity (E. Field et al., 2013), whether such scaling applies to individual fault segments and/or their immediate surroundings is a topic of active research (Wesnousky, 1994; Ishibe & Shimazaki, 2012; Kagan et al., 2012; Page & Felzer, 2015; Page & van der Elst, 2018; E. H. Field et al., 2017). Estimates of b-values associated with individual fault segments can exhibit considerable variability (e.g. between 0.5 and 1.5 along faults in California; Tormann et al., 2014), and are sensitive to a number of factors, including the magnitude of completeness of the relevant earthquake catalog and the choice of observation region and time window (Tormann et al., 2014; Page & Felzer, 2015; Ishibe & Shimazaki, 2012; Page & van der Elst, 2018). A number of studies suggest that the rate of large earthquakes on major faults, such as the San Andreas Fault, is elevated above what would be expected given typical Gutenberg-Richter scaling from smaller magnitude events (Schwartz & Coppersmith, 1984; E. H. Field et al., 2017). In particular, some mature fault segments that have historically hosted large earthquakes, such as the Cholame and Carrizo segments of the San Andreas Fault, exhibit substantial deviations from typical Gutenberg-Richter scaling, being nearly absent of small earthquakes (Sieh, 1978; Wesnousky, 1994; Bouchon & Karabulut, 2008; Hauksson et al., 2012; Jiang & Lapusta, 2016; Michailos et al., 2019). Our findings suggest that the paucity of microseismicity on such mature fault segments may indicate that they undergo substantial dynamic weakening during earthquakes ruptures.

8 Discussion

Our simulations demonstrate that the average shear prestress required for rupture propagation can be considerably lower than the average shear stress required for the rupture nucleation. This is because the quasi-static nucleation process is governed by relatively small stress changes and hence requires favorable prestress conditions - close to the local steady-state quasi-static shear resistance - to proceed. In contrast, during dynamic rupture, the rupture front is driven by larger wave-mediated dynamic stress concentrations, which are more substantial for larger ruptures and facilitate rupture propagation over less favorably stressed regions, resulting in the spatially-averaged prestress over the ruptured area being much lower than the average local SSQS shear resistance. More efficient weakening facilitates larger dynamic stress changes at the rupture front, allowing propagation over even less favorable prestress conditions. Our results highlight the significance of heterogeneity in prestress, or shear resistance, for the nucleation and ultimate arrest of finite ruptures, even in fault models that have otherwise uniform material and confining properties.

The decrease in averaged prestress with rupture length can be interpreted as a decrease in the average quasi-static friction coefficient $\tau^A_{\text{ini}}/(\sigma - p_{\text{int}})$ with rupture size (Figure 7). The average quasi-static friction coefficients for ruptures on the scale of the nucleation size are consistent with the prescribed quasi-static reference friction coefficient near typical Byerlee values. However, as we average the prestress over larger rupture lengths, the average quasi-static friction coefficient can considerably decrease depending on the efficiency in weakening.

The presence of enhanced dynamic weakening draws the average shear stress along larger regions of the fault below the local SSQS consistent with earthquake nucleation, resulting in lower average shear stress conditions in terms of both the average prestress for larger ruptures and the average dynamic resistance associated with shear heating during ruptures (Figure 11). The models presented in this study with mild-to-moderate enhanced weakening include considerable persistent fluid overpressurization to maintain low-heat, low-stress conditions with average dynamic shear resistance during seismic slip rates below 10 MPa; however the degree of fluid overpressure required to maintain low-heat conditions is less than that with comparable rate-and-state properties but no enhanced weakening. The presence of some enhanced dynamic weakening is also needed for persistently weak fault models due to chronic fluid overpressure in order to ensure that static stress drops are not too small, as they would otherwise be with low effective stress and small changes in the friction coefficient due to standard rate-and-state laws (Figures 11 and S3; Lambert et al., in press). Fault models with more efficient dynamic weakening have been shown to be able to reproduce low-stress operation and reasonable static stress drops with quasi-static friction coefficients around Byerlee values and higher effective normal stress (e.g. ≥ 100 MPa; Noda et al., 2009; Dunham et al., 2011; Lambert et al., in press). Earthquake sequence simulations of such fault models typically consist of only large ruptures (Lambert et al., in press), consistent with the notion that large fault areas governed by efficient weakening maintain substantially lower average shear stresses than that required for nucleation. These findings further strengthen the conclusion of prior studies that enhanced dynamic weakening can help explain the discrepancy between laboratory values of (quasi-static) friction coefficients around 0.6 and geophysical inferences of low effective coefficients of friction (< 0.2), along with mild average static stress drops of 1 to 10 MPa, over fault areas that host large earthquakes (e.g Marone, 1998; Suppe, 2007; Allmann & Shearer, 2009; Noda et al., 2009; Dunham et al., 2011; Ikari et al., 2011; Gao & Wang, 2014; Ye et al., 2016b; Perry et al., 2020; Lambert et al., in press).

The scale dependence of average prestress before ruptures can also be interpreted as a scale dependence of *average fault strength*, since the average prestress represents a measure of how much shear stress that fault region can hold before failing in a rupture. Given this interpretation, our simulations suggest that faults maintain lower average shear stresses, and hence appear weaker, at larger scales than at smaller scales. This interpretation is conceptually consistent with laboratory measurements of scale-dependent yield stress for rocks and a number of engineering materials, which demonstrate decreasing material strength with increasing scale (Jaeger & Cook, 1976; Bandis et al., 1981; Greer et al., 2005; Pharr et al., 2010; Uchic et al., 2004; Yamashita et al., 2015; Thom et al., 2017). Note that our larger simulated ruptures, even with more efficient weakening, still require higher average shear stresses over smaller scales in order to nucleate and grow.

Thus the lower average prestress levels that allow continued failure in dynamic ruptures at larger scales only become relevant once the rupture event has already nucleated and sufficiently grown over smaller scales. This consideration suggests that the critical stress conditions for rupture occurrence are governed not by a single stress quantity but by a distribution of scale-dependent stress criteria for rupture nucleation and continued propagation. An important implication of our findings is that the critical stress for earthquake occurrence may not be governed by a simple condition such as a certain level of Coulomb stress. Given our findings, in order to reason about the stress conditions critical for a rupture to occur, it is important to consider both the size of the rupture and the weakening behavior, and hence the style of motion, that may occur throughout rupture propagation.

The scale dependence of fault material strength has also been hypothesized to explain the measured scaling of roughness on natural fault surfaces (Brodsky et al., 2016). Dynamic rupture simulations on geometrically irregular faults motivated by such roughness measurements have indicated an additional contribution to fault shear resistance arising from roughness drag during rupture propagation (Fang & Dunham, 2013). Further examination of the scale dependence of average shear resistance across faults including realistic fault geometry is an important topic for future work.

A common assumption is that the shear prestress over the entire ruptured area must be near the local static (or quasi-static) strength, comparable to the SSQS shear resistance discussed in this study. We demonstrate that the assumption is not necessarily valid and that faults with enhanced dynamic weakening and history of large earthquake ruptures would, in fact, be expected to have low average shear stress over large enough scales. At the same time, the state of stress needs to be heterogeneous, with the average stresses over small scales (comparable to earthquake nucleation) being close to the (much higher) local SSQS shear resistance in some places. Thus, while individual measurements of low resolved shear stress onto a fault may suggest that those locations appear to not be critically stressed for quasi-static failure, those regions, and much of the fault, may be sufficiently stressed to sustain dynamic rupture propagation and hence large earthquake ruptures. In addition, our findings suggest that inferences of stress levels on faults may differ if they are obtained over different scales or influenced by different rupture processes. For example, low-stress conditions on mature faults from observations of low heat flow may not only represent average shear stress conditions over large fault segments as a whole but also be dominated by low dynamic resistance during fast slip, whereas averages over smaller scales would be expected to reflect the heterogeneity of the underlying prestress distribution, as perhaps reflected in varying stress rotations inferred over scales of tens of kilometers (Hardebeck & Hauksson, 1999, 2001; Hardebeck, 2015).

Our modeling shows that increasingly efficient dynamic weakening leads to different earthquake statistics, with fewer small events and increasing number of large events. Another factor that can significantly affect the ability of earthquake ruptures to propagate is fault heterogeneity. Some dynamic heterogeneity in shear stress spontaneously develops in our simulations, leading to a broad distribution of event sizes for cases with mild to moderate enhanced dynamic weakening. Our findings suggest that the effects of pre-existing types of fault heterogeneity need to be considered with respect to the size of the rupture and weakening behavior on the fault. For example, faults that experience more substantial weakening would require the presence of larger amplitudes of small-wavelength heterogeneity in shear stress or resistance to produce small events. Examining the relationship between earthquake sequence complexity and varying levels of fault heterogeneity and enhanced dynamic weakening is an important topic for future work.

9 Conclusions

Our modeling of faults with rate-and-state friction and enhanced dynamic weakening indicates that average shear prestress before dynamic rupture - which can serve as a measure of average fault strength - can be scale-dependent and decrease with the increasing rupture size. Such decrease is more prominent for faults with more efficient dynamic weakening. The finding holds for faults with the standard rate-and-state friction only, without any additional dynamic weakening, although the dependence is relatively unremarkable in that case (Figures 7 and S4). However, the scale-dependent decrease in average prestress is quite pronounced even for fault models with mild to moderate enhanced dynamic weakening that satisfy a number of other field inferences, including nearly magnitude-invariant static stress drops of 1-10 MPa, increasing average breakdown energy with rupture size, radiation ratios between 0.1 and 1.0, and low-heat fault operation (Perry et al., 2020; Lambert et al., in press).

Our simulations illustrate that both critical fault stress required for rupture propagation and static stress drops are products of complex finite-fault interactions, including wave-mediated stress concentrations at the rupture front and redistribution of stress post-rupture by dynamic waves. Hence it is important to keep in mind the finite-fault effects - and their consequences in terms of the spatially variable fault prestress, slip rate, and shear stress evolution - when interpreting single-degree-of-freedom representations, such as spring-slider models and small-scale laboratory measurements. This consideration highlights the need to continue developing a better physical understanding of faulting at various scales through a combination and interaction of small-scale and intermediate-scale lab and field experiments, constitutive relations formulated based on such experiments, and finite-fault numerical modeling constrained by inferences from large-scale field observations. Our comparison of local fault behavior in SDOF and dynamic rupture simulatons also demonstrate how small-scale experiments can be used in conjunction with finite-fault modeling to improve our understanding of the earthquake source: the finite-fault modeling can suggest the initial conditions and slip-rate histories for the small-scale experiments to impose, and then the shear stress evolution from the small-scale experiments can be compared to the numerically obtained ones, which would allow to validate and improve the constitutive laws used in finite-fault modeling.

We find that increasingly efficient dynamic weakening leads to different earthquake statistics, with fewer small events and increasingly more large events. This finding is consistent with the interpretation of average fault prestress before rupture as average fault strength, in that lower fault strength over larger scales leads to an increasing number of larger events. It also adds to the body of work suggesting that enhanced dynamic weakening may be responsible for deviations - inferred for large, mature fault segments - of earthquake statistics from the Gutenberg-Richter scaling (Sieh, 1978; Bouchon & Karabulut, 2008; Hauksson et al., 2012; Jiang & Lapusta, 2016; Michailos et al., 2019). For example, fault models with efficient dynamic weakening are consistent with mature faults that have historically hosted large earthquakes but otherwise appear seismically quiescent, such as the Cholame and Carrizo segments of the San Andreas Fault, which hosted the 1857 Fort Tejon earthquake (Jiang & Lapusta, 2016).

Such considerations may be useful for earthquake early warning systems, which currently do not take into account the potential physics-based differences in the event size distribution. Under the assumption of Gutenberg-Richter statistics, the probability that a smaller, Mw 5 or 6 event becomes a much larger earthquake is not great; however, that probability may be substantially larger on mature faults if they are indeed governed by enhanced dynamic weakening.

Our results indicate that critical stress conditions for earthquake occurrence cannot be described by a single number but rather present as complex spatial distribution with scale-dependent averages. When considering the critical stress conditions, it is essential to take into account both the size of the rupture and the weakening behavior, and hence the style of motion, that may occur throughout rupture propagation. These results warrant further investigation, specifically how the weakening behavior during dynamic rupture would interact with different degrees of fault heterogeneity as well as implications for earthquake early warning.

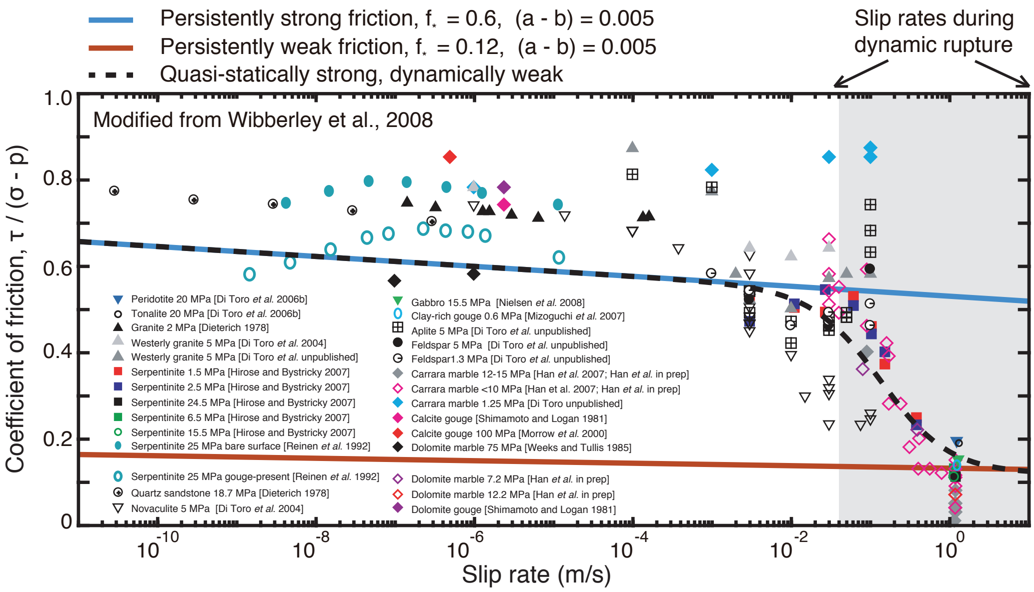

Figure 1. Field observations suggest that the average effective friction on mature faults must be low (< 0.1). One explanation for this inferred low effective friction would be that mature faults are persistently weak, such as from the presence of fault materials with persistently low friction coefficients $\tau/(\sigma - p)$ (red). Faults may also be persistently weak while having actual friction coefficients that are persistently high (> 0.2, blue), but require substantial chronic fluid overpressure in order to maintain low effective fault friction. A number of laboratory experiments indicate that the coefficient of friction for many materials relevant to seismogenic faults is around 0.6-0.8 at low sliding rates, but drops dramatically to lower values (< 0.2) at higher slip rates relevant to seismic slip, consistent with the notion of quasi-statically strong, but dynamically weak behavior (dashed black line).

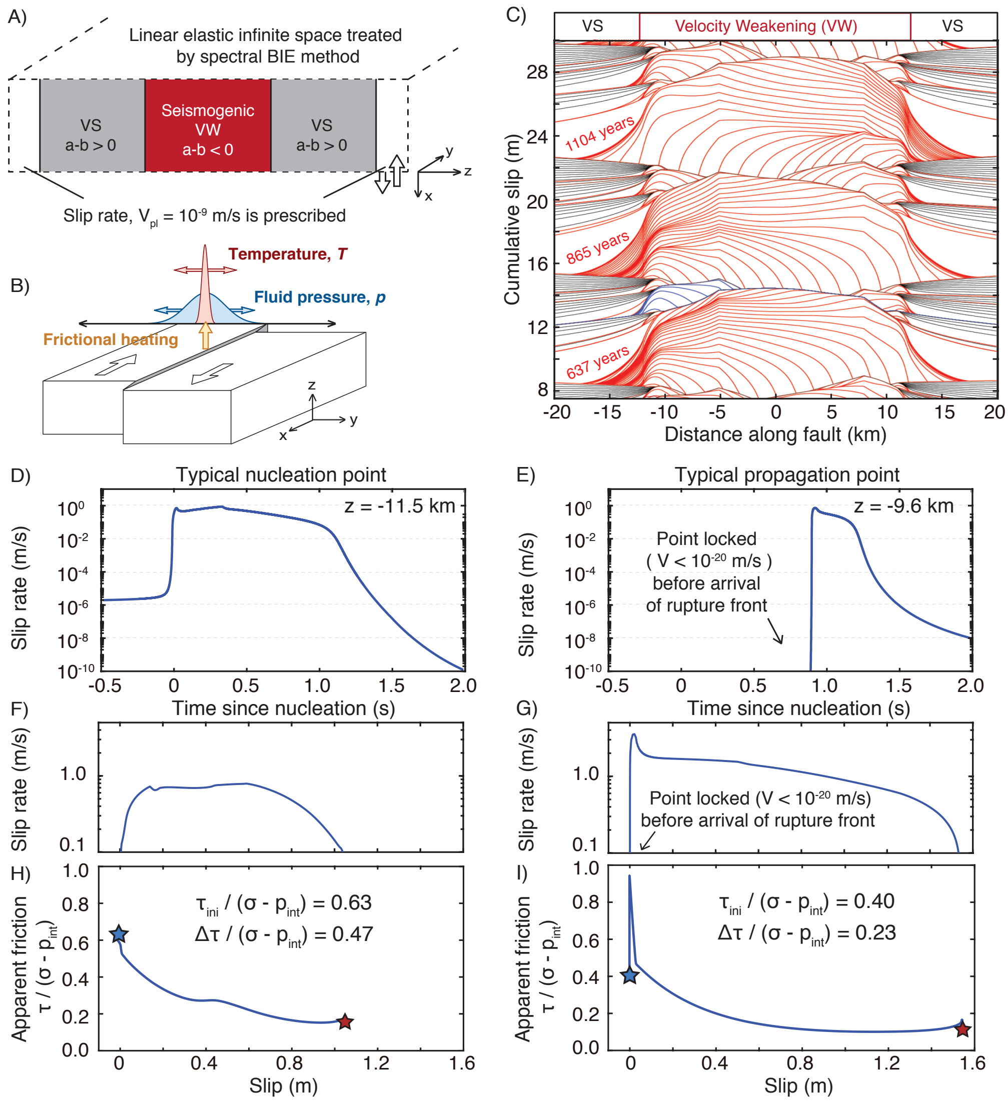

Figure 2. Modeling of sequences of earthquakes and aseismic slip on a rate-and-state fault with (A) a velocity-weakening (VW) seismogenic region surrounded by two velocity-strengthening (VS) sections and (B) enhanced dynamic weakening due to the thermal pressurization of pore fluids. The evolution of temperature and pore fluid pressure due to shear heating and off-fault diffusion is computed throughout our simulations. (C) A short section of the accumulated slip history in fault model TP3 (Table 2). Seismic events are illustrated by red lines plotted every 0.5 s while aseismic slip is shown by black lines plotted every 10 years. (D-G) Evolution of local slip rate with time and slip at points representative of nucleation and typical rupture propagation behavior within a crack-like rupture (colored blue in C). Points throughout rupture propagation (E & G) are initially locked and are driven to rupture by the concentration of dynamic stresses at the rupture front, thus experiencing more rapid acceleration of slip compared to points within the nucleation region (D & F). (H-I) The difference in local slip rate history contributes to a difference in the evolution of shear stress with slip. (H) Evolution of the apparent coefficient of friction $\tau/(\sigma - p_{\rm int})$ with slip in the nucleation region is consistent with the laboratory notion of quasi-statically strong, dynamically weak behavior, with the apparent friction coefficient initially close to the reference value of 0.6 and dropping to a low dynamic resistance below 0.2 with slip. (I) Evolution of the apparent friction coefficient at points throughout rupture propagation is more complicated as the scaled prestress can be much lower than the reference friction before the arrival of the dynamic stress concentration.

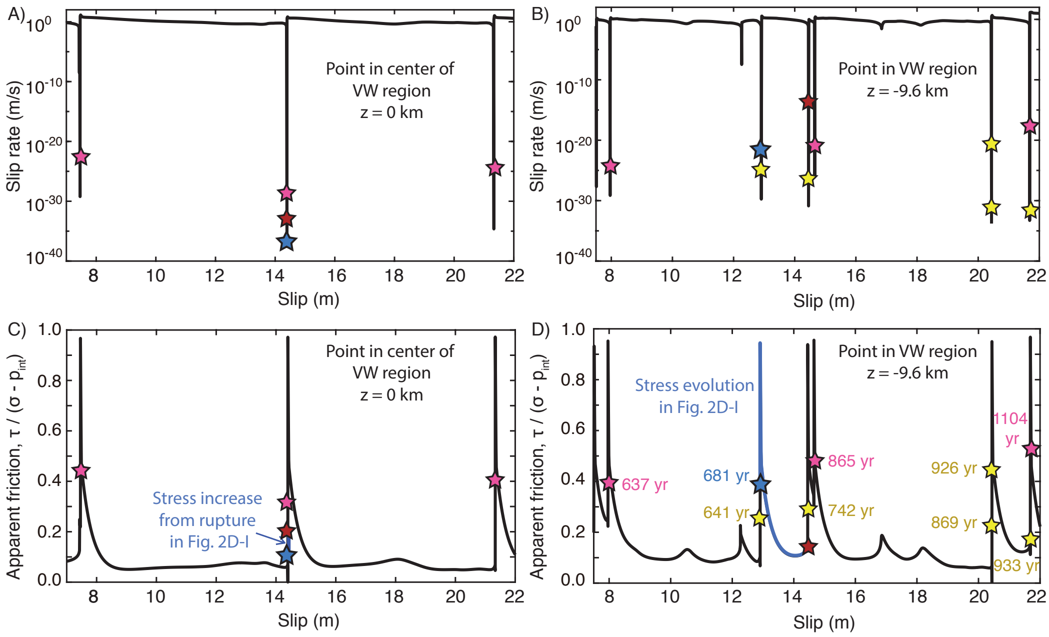

Figure 3. Evolution of the local slip rate and apparent friction coefficient at points within the velocity-weakening (VW) region with accumulating slip in fault model TP3 (Table 2). The stars denote instances in the earthquake sequence in Figure 2C, with pink stars marking the initiation of the three large model-spanning ruptures, the blue and red stars denoting the beginning and end of the moderate-sized rupture illustrated by blue contours, respectively. The yellow stars denote small to moderate-sized ruptures occurring along the VW-VS boundary at $z = -12$ km. (A & C) The point in the center of the VW region (z = 0 km) ruptures and experiences substantial slip only in large ruptures. The point exhibits an increase in shear stress over time due to the stress transfer from smaller ruptures that do not penetrate into the center of the VW region (such as the rupture colored blue in Fig. 2C). (B & D) Points closer to the boundary between the VW and VS regions can rupture during both smaller and large ruptures depending on the pre-stress conditions when ruptures arrive, resulting in a more complicated evolution of shear stress with accumulating slip. For both points in the VW region, the shear stress is brought to the peak stress and failure during ruptures by the dynamic stresses at the rupture front.

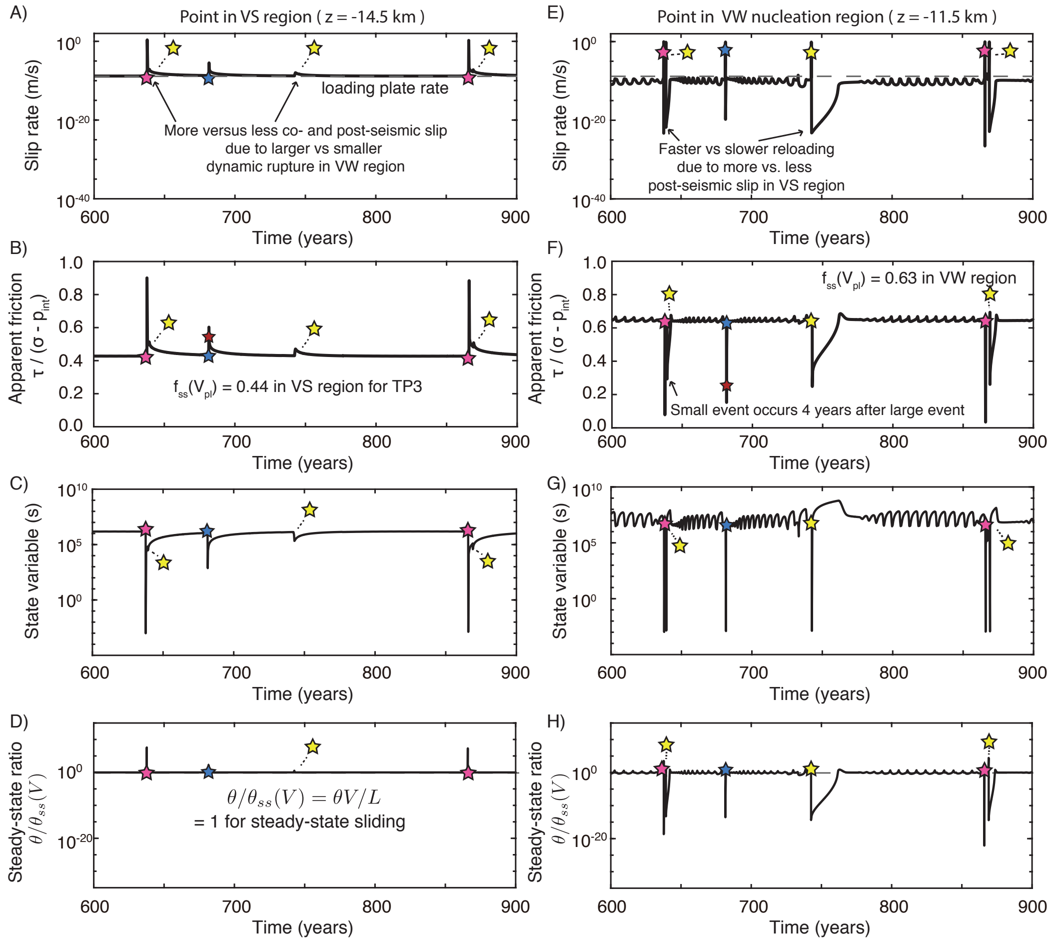

Figure 4. Evolution of local slip rate, apparent friction, and state variable at points near rupture nucleation between two model-spanning ruptures. The stars denote instances in the earthquake sequence in Figure 2C, with pink stars marking the initiation of the first two large model-spanning ruptures, the blue star denoting the beginning of the moderate-sized rupture illustrated by blue contours and the yellow stars denoting smaller ruptures. (A) Points within the VS region typically slip near the loading plate rate but can experience transient accelerated slip during and following ruptures occurring within the VW region. (B-D) The apparent friction coefficient and state variable in the VS region is typically near steady state, except during accelerated slip. (E-F) Slow slip penetrates into the VW region, driving points near the VW-VS boundary close to the loading slip rate, with the apparent friction coefficient being close to the corresponding steady-state value $f_{\text{ss}}(V_{\text{pl}})$. The slip rate and apparent friction exhibit small oscillations as the points near the VW-VS boundary continue to be loaded by slow slip in the VS region, accelerate, and weaken, thus transmitting stress further into the VW region until a sufficiently large region is loaded to sustain rupture nucleation and acceleration to seismic slip rates. The loading rate of the VW region also depends on the amount of accelerated slip in the VS due to previous ruptures (e.g. A & E around 650 vs. 750 years). (G-H) Following dynamic rupture, the state variable heals close to the steady-state value around the prescribed loading rate $\theta_{ss}(V_{\text{pl}})$ but continues to oscillate along with the unsteady slip resulting from the penetration of creep into the VW region, as seen in (E).

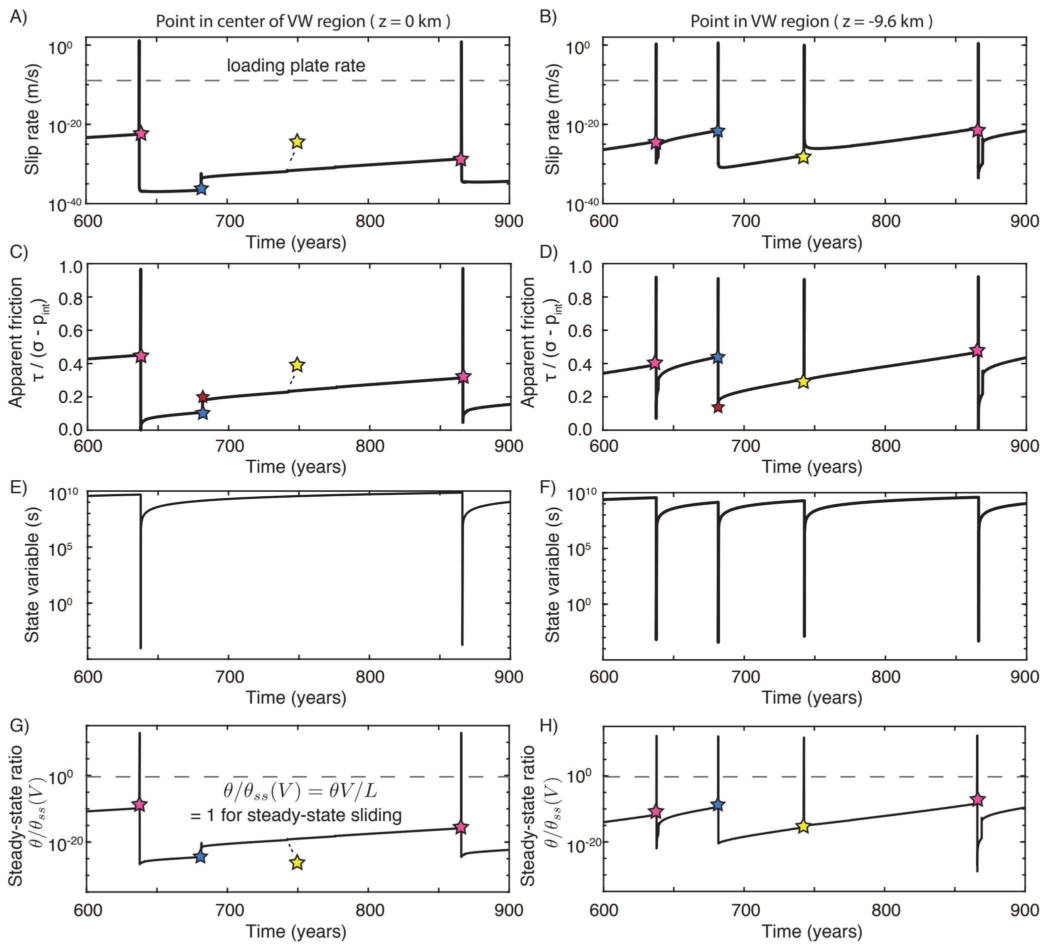

Figure 5. Evolution of local slip rate, apparent friction, and state variable at points within the VW region between two model-spanning ruptures. The stars denote instances in the earthquake sequence in Figure 2C, with pink stars marking the initiation of the first two large model-spanning ruptures, the blue star denoting the beginning of the moderate-sized rupture illustrated by blue contours and the yellow stars denoting smaller ruptures. (A-B) Points within the VW region are typically locked in between earthquake ruptures, sliding at slip rates far below the loading plate rate. (C-D) Loading from the VS regions as well as slip in neighboring ruptures leads to a time-dependent increase in shear stress. However, the points are still near-locked when dynamic rupture arrives from elsewhere, bringing a significant stress concentration and weakening on the timescale of the event which here collapses onto a vertical line. (E-F) The evolution of the state variable shows increase in the interseismic periods which encapsulate the fault healing and decrease to low values during earthquake rupture. (G-H) The ratio of the current value of the state variable θ to the steady-state value $\theta_{ss}(V)$, corresponding to the current local slip rate V, is much smaller than 1 during the interseismic periods, indicating the continued healing of shear resistance prior to rupture. As the slip rate rapidly accelerates during dynamic rupture, the state variable temporarily exceeds the new much lower steady-state values corresponding to the dynamic slip rate $\theta_{ss}(V_{\text{dyn}})$, then evolves to this lower steady-state value, and then falls to values below steady-state during the interseismic periods, indicating fault healing.

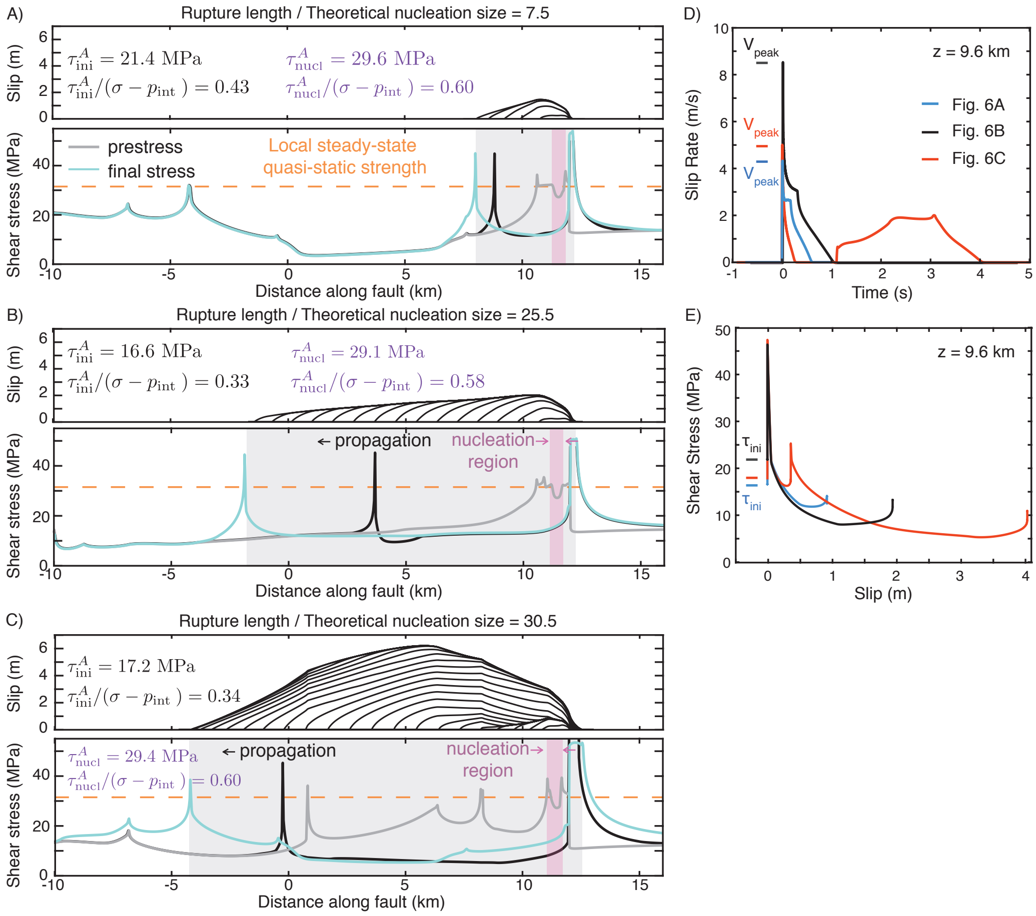

Figure 6. Spatial distribution of slip (top) and prestress and final shear stress (bottom) during three ruptures (A-C) with different rupture lengths in the same fault model (TP4 from Table 2). Slip contours are plotted every 0.25 s. The purple and gray shading illustrates the extent of the nucleation and ruptured regions, respectively, over which the prestress is averaged. While the ruptures nucleate in regions with stress levels near the local steady-state quasi-static shear resistance (dashed orange line), larger ruptures propagate over lower prestressed areas, resulting in lower average prestress and lower average coefficients of friction $\tau^A_{\rm ini}/[\sigma - p_{\rm int}]$. The shear stress distribution for a typical moment during rupture propagation is shown in black, demonstrating the stress concentration at the rupture front that brings the fault stress to values comparable to the SSQS shear resistance. The peak stress is even higher since the fault is initially dynamically stronger due to the rate-and-state direct effect. (D-E) Significant differences in local evolution of slip and stress at the same fault location ($z = 9.6$ km) for different ruptures that depend on the prestress conditions due to previous slip events and the dynamic stress interactions during the individual ruptures.

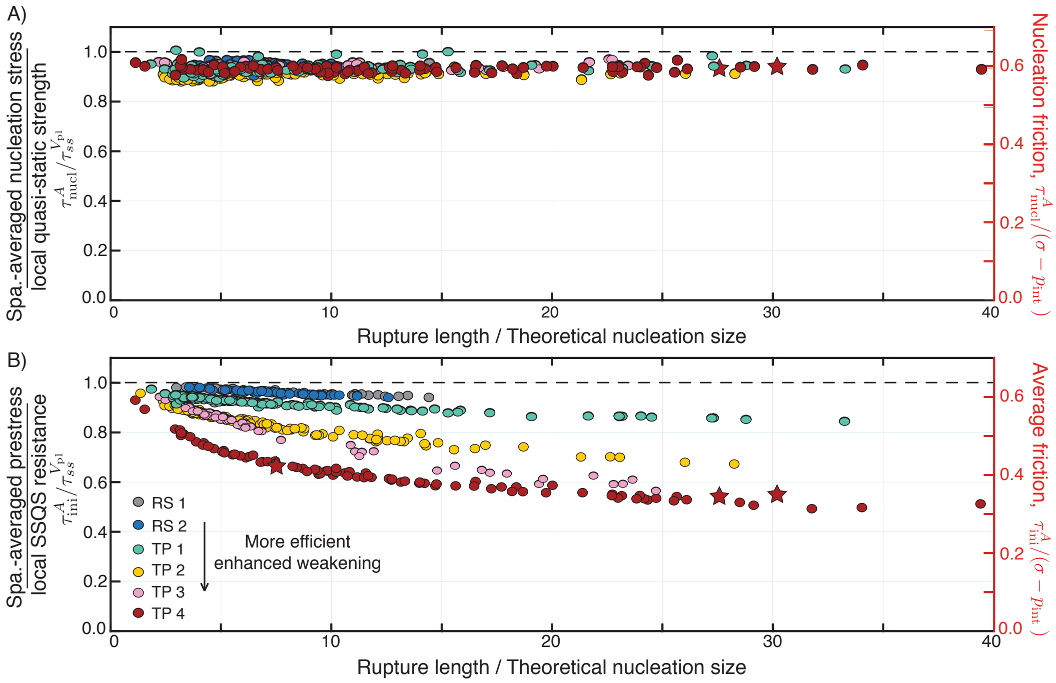

Figure 7. The difference between average shear stress needed for rupture nucleation vs. dynamic propagation. (A) The spatially-averaged nucleation stress τ^A_{nucl} for ruptures is comparable to the average local steady-state quasi-static shear resistance $\tau^{V_{\mathrm{pl}}}_{ss}$, regardless of the final rupture size. (B) The spatially-averaged prestress τ^A_{ini} and average friction coefficient $\tau^A_{\mathrm{ini}}/(\sigma - p_{\mathrm{int}})$ decrease with increasing rupture size; the effect is more pronounced with increasing efficiency of weakening. The three ruptures shown in Figure 6 are denoted by red stars.

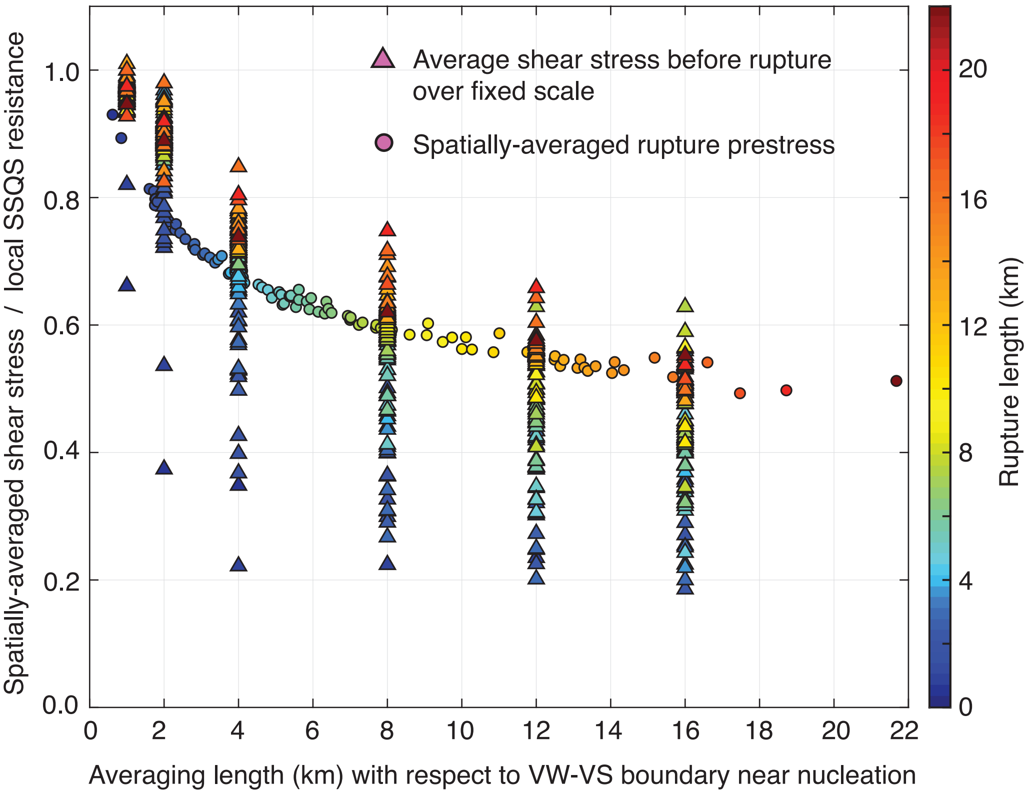

Figure 8. Comparison of the spatially averaged prestress over several fixed scales (1, 2, 4, 8, 12, and 16 km) and the average prestress over ruptures of varying size. As shown in Figure 7, the spatially-averaged prestress over the total rupture area τ_{ini}^{A} (circles) decreases considerably with rupture size in fault model TP4 from Table 2 with moderate enhanced dynamic weakening. However, larger ruptures have generally higher average shear stresses over smaller fixed scales around the nucleation region compared to smaller ruptures (red vs. blue triangles). The spatially-averaged shear stress over 1 km from the VW-VS boundary near the nucleation region of ruptures (triangles on the far-left) is relatively high (comparable to the local SSQS resistance) for both small and large ruptures, indicating that ruptures nucleate in regions of relatively high prestress compared to the average prestress over the entire rupture area (circles). For smaller ruptures, the average prestress at the fixed scales just larger than their total rupture length is lower than the average prestress of ruptures with comparable length to the fixed scale, suggesting that the prestress levels were too low to sustain further rupture propagation.

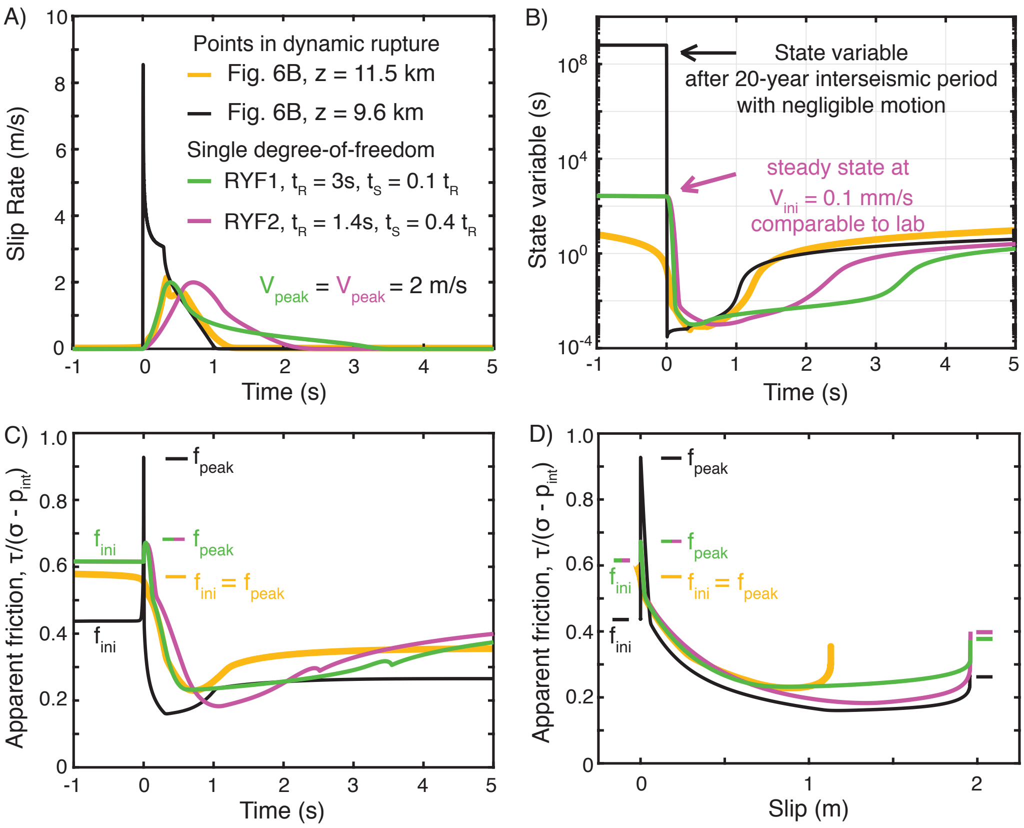

Figure 9. Comparison of the results of our dynamic modeling with what would be obtained in laboratory experiments given the same constitutive properties and typical lab procedures. (A) Comparison of the local slip rate during nucleation ($z = 11.5$ km, yellow) and typical propagation ($z = 9.6$ km, black) of the simulated dynamic rupture of Figure 6B with the slip rate evolution that could be imposed in lab experiments represented by two regularized Yoffe functions (Tinti et al., 2005) with peak slip rate of 2 m/s and comparable slip to the point at $z = 9.6$ km. The imposed regularized Yoffe functions are generally comparable to the evolution of slip within the nucleation region ($z = 11.5$ km), however they do not capture the rapid acceleration of slip associated with the arrival of the rupture front at points of typical propagation, as observed at $z = 9.6$ km. (B) Comparison of the state variable evolution from our simulation and the lab experiment which we simulate using the single-degree of freedom (SDOF) equations. The simulated lab experiment starts with the steady-state conditions for 0.1 mm/s based on the experiments of Fukuyama and Mizoguchi (2010), which results in a much lower initial state value compared to the point $z = 9.6$ km in our simulations which, prior to dynamic rupture, had negligible motion over a 20-year interseismic period. (C-D) Evolution of the local apparent coefficient of friction with time and slip for the point in our simulated finite-fault dynamic rupture and SDOF lab experiments. The dynamic weakening is generally comparable between the points in the finite rupture and the SDOF experiments, however the evolution of shear stress substantially differ with regards to the much lower prestress at $z = 9.6$ km before the finite dynamic rupture and the abrupt increase and then decrease in stress due to the arrival of the dynamic rupture front and the associated rapid weakening.

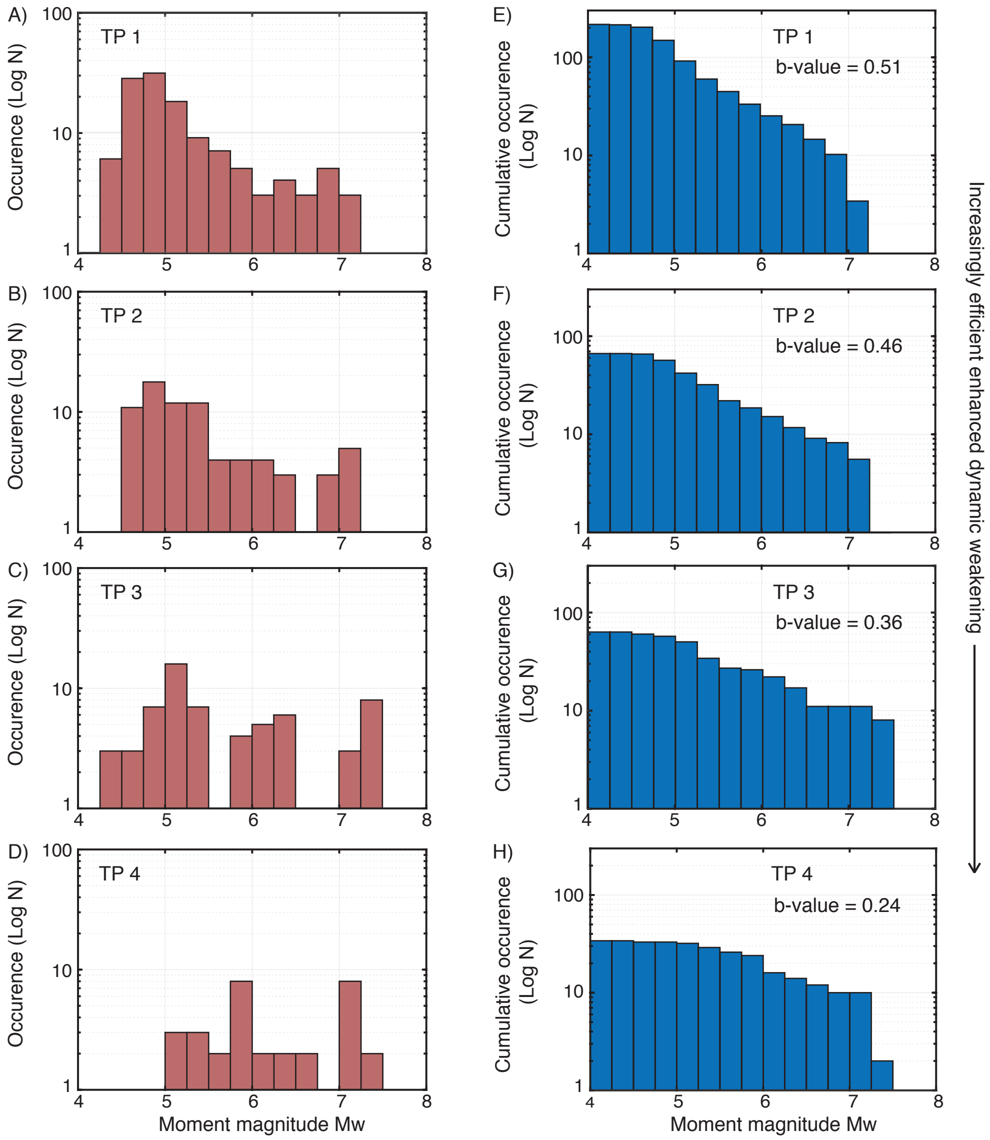

Figure 10. Fault models with more efficient weakening result in less earthquake sequence complexity, producing fewer smaller events (left column) and smaller b-values (right column). (A-D) Frequency-magnitude and (E-H) cumulative frequency-magnitude statistics for simulations with increasing efficiency of enhanced dynamic weakening (TP1-4 from Table 2).

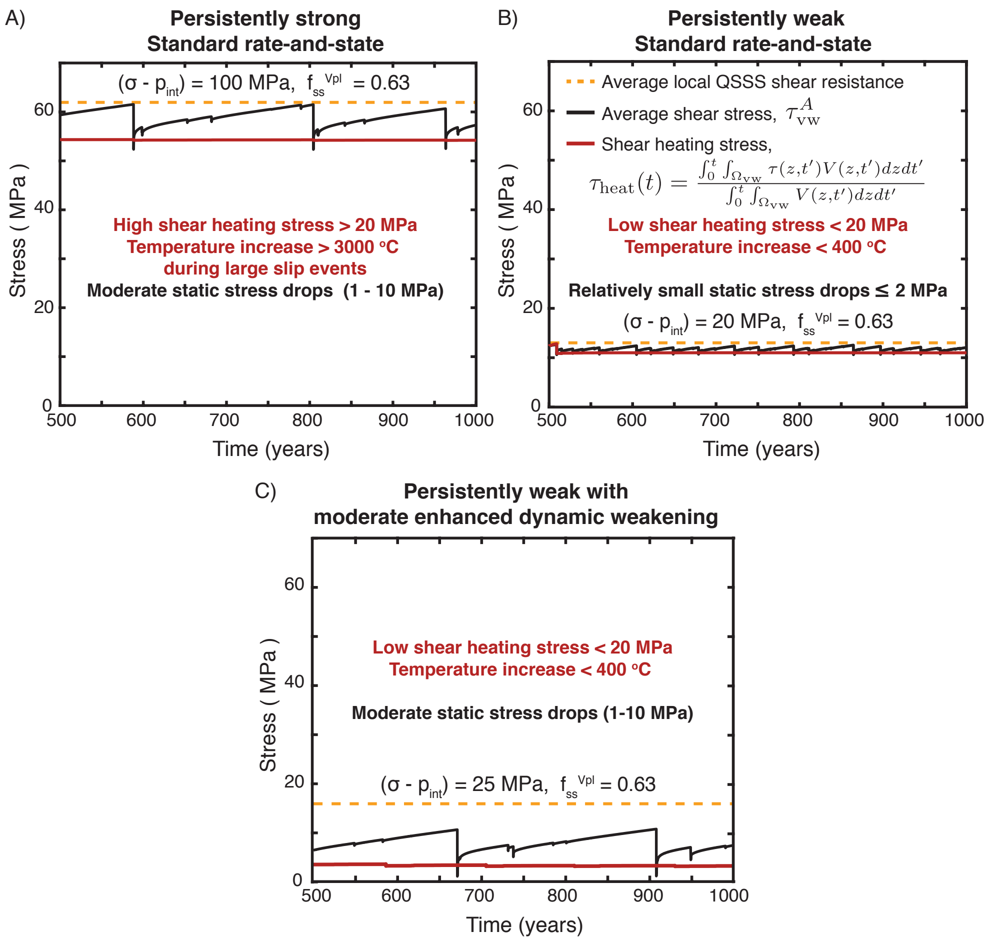

Figure 11. Evolution of the spatially averaged shear stress in the VW region τ^A_{vw} (black line) over earthquakes sequences. (A-B) Standard rate-and-state friction results in modest changes in shear resistance from the average local steady-state quasi-static (SSQS) shear resistance (orange line). Ruptures on persistently strong faults produce realistic static stress drops (A); however, the fault temperature would increase by more than 3000 ^{o}C during a dynamic event for a shear-zone half-width of 10 mm. (B) Persistently weak fault models due to low effective normal stress but with no enhanced weakening (RS 1 of Table 2) can maintain modest fault temperatures, but produce relatively small static stress drops $\leq$ 2 MPa. (C) Persistently weak models with mild to moderate enhanced dynamic weakening (TP3 of Table 2) are capable of maintaining modest fault temperatures and producing more moderate average stress drops between 1 - 10 MPa.

Parameter	Symbol	Value
Loading slip rate	V_{pl}	10^{-9} m/s
Shear wave speed	c_s	3299 m/s
Shear modulus	μ	36 GPa
Thermal diffusivity	α_{th}	10^{-6} m^2/s
Specific heat	ρc	2.7 MPa/K
Shear zone half-width	w	10 mm
Rate-and-state parameters		
Reference slip velocity	V_*	10^{-6} m/s
Reference friction coefficient	f_*	0.6
Rate-and-state direct effect (VW)	a	0.010
Rate-and-state evolution effect (VW)	b	0.015
Rate-and-state evolution effect (VS)	b	0.003
Length scales		
Fault length	λ	96 km
Frictional domain	λ_{fr}	72 km
Velocity-weakening region	λ_{VW}	24 km
Cell size	Δz	3.3 m
Quasi-static cohesive zone	Λ_0	84 m
Nucleation size (Rice & Ruina, 1983)	h^*_{RR}	226 m
Nucleation size (Rubin & Ampuero, 2005)	h^*_{RA}	550 m

Table 1. Model parameters used in all simulations unless otherwise specified.

Parameter	Symbol	TP 1	TP 2	TP 3	TP 4
Interseismic effective normal stress (MPa)	$\bar{\sigma} = (\sigma - p_{\text{int}})$	25	25	25	50
Rate-and-state direct effect (VS)	a	0.050	0.050	0.025	0.050
Characteristic slip (mm)	L	1	1	1	2
Coupling coefficient (MPa/K)	Λ	0.1	0.34	0.34	0.34
Hydraulic diffusivity m^2/s	α_{hy}	10^{-3}	10^{-3}	10^{-4}	10^{-3}

Table 2. Parameters for models including thermal pressurization of pore fluids.

Parameter	Symbol	RS 1	RS 2
Interseismic effective normal stress (MPa)	$\bar{\sigma} = (\sigma - p_{\text{int}})$	20	10
Rate-and-state direct effect (VS)	a	0.050	0.050
Characteristic slip (mm)	L	1	0.5
Quasi-static cohesive zone (m)	Λ_0	106	106
Nucleation size (m), Rice & Ruina, 1983	h^*_{RR}	282	282
Nucleation size (m), Rubin & Ampuero, 2005	h^*_{RA}	688	688

Table 3. Parameters for models including only standard rate-and-state friction.

Acknowledgments

This study was supported by the National Science Foundation (grants EAR 1724686) and the Southern California Earthquake Center (SCEC), contribution No. 10782. SCEC is funded by NSF Cooperative Agreement EAR-1033462 and USGS Cooperative Agreement G12AC20038. D. Faulkner was supported by the Natural Environment Research Council (grants NE/P002943/1 and NE/R017484/1). The numerical simulations for this work were done on the High Performance Computing Central cluster of the California Institute of Technology. The data supporting the analysis and conclusions is given in Figures and Tables, in the main text and supplementary materials. Data is accessible through the CaltechDATA repository (https://data.caltech.edu/records/1612). We thank Tom Heaton, Hiroo Kanamori, and Emily Brodsky for helpful discussions.

References

Acosta, M., Passelègue, F. X., Schubnel, A., & Violay, M. (2018). Dynamic weakening during earthquakes controlled by fluid thermodynamics. *Nature Communications*, *9*(1), 3074. doi: 10.1038/s41467-018-05603-9

Ader, T. J., Lapusta, N., Avouac, J.-P., & Ampuero, J.-P. (2014, 05). Response of rate-and-state seismogenic faults to harmonic shear-stress perturbations. *Geophysical Journal International*, *198*(1), 385-413. Retrieved from `https://doi.org/10.1093/gji/ggu144` doi: 10.1093/gji/ggu144

Allmann, B. P., & Shearer, P. M. (2009). Global variations of stress drop for moderate to large earthquakes. *Journal of Geophysical Research: Solid Earth*, *114*(B1). doi: 10.1029/2008JB005821

Bandis, S., Lumsden, A., & Barton, N. (1981). Experimental studies of scale effects on the shear behaviour of rock joints. *International Journal of Rock Mechanics and Mining Sciences & Geomechanics Abstracts*, *18*(1), 1 - 21. doi: https://doi.org/10.1016/0148-9062(81)90262-X

Bangs, N., Moore, G., Gulick, S., Pangborn, E., Tobin, H., Kuramoto, S., & Taira,

A. (2009). Broad, weak regions of the Nankai Megathrust and implications for shallow coseismic slip. *Earth and Planetary Science Letters*, *284*(1), 44 - 49.

Ben-David, O., Cohen, G., & Fineberg, J. (2010). The dynamics of the onset of frictional slip. *Science*, *330*(6001), 211–214. doi: 10.1126/science.1194777

Bhattacharya, P., Rubin, A. M., & Beeler, N. M. (2017). Does fault strengthening in laboratory rock friction experiments really depend primarily upon time and not slip? *Journal of Geophysical Research: Solid Earth*, *122*(8), 6389-6430. doi: https://doi.org/10.1002/2017JB013936

Bouchon, M., & Karabulut, H. (2008). The aftershock signature of supershear earthquakes. *Science*, *320*(5881), 1323–1325. doi: 10.1126/science.1155030

Brodsky, E. E., Kirkpatrick, J. D., & Candela, T. (2016, 01). Constraints from fault roughness on the scale-dependent strength of rocks. *Geology*, *44*(1), 19-22. doi: 10.1130/G37206.1

Brown, K., Kopf, A., Underwood, M., & Weinberger, J. (2003). Compositional and fluid pressure controls on the state of stress on the Nankai subduction thrust: A weak plate boundary. *Earth and Planetary Science Letters*, *214*(3), 589 - 603.

Brune, J. N., Henyey, T. L., & Roy, R. F. (1969). Heat flow, stress, and rate of slip along the San Andreas Fault, California. *Journal of Geophysical Research*, *74*(15), 3821-3827.

Byerlee, J. (1978). Friction of rocks. *Pure and Applied Geophysics*, *116*(4-5), 615-626. doi: 10.1007/BF00876528

Cattania, C. (2019). Complex earthquake sequences on simple faults. *Geophysical Research Letters*, *46*(17-18), 10384-10393. doi: 10.1029/2019GL083628

Chen, J., Verberne, B. A., & Spiers, C. J. (2015a). Effects of healing on the seismogenic potential of carbonate fault rocks: Experiments on samples from the longmenshan fault, sichuan, china. *Journal of Geophysical Research: Solid Earth*, *120*(8), 5479-5506. doi: https://doi.org/10.1002/2015JB012051

Chen, J., Verberne, B. A., & Spiers, C. J. (2015b). Interseismic re-strengthening and stabilization of carbonate faults by "non-dieterich" healing under hydrothermal conditions. *Earth and Planetary Science Letters*, *423*, 1 - 12. doi: https://doi.org/10.1016/j.epsl.2015.03.044

Collettini, C., Niemeijer, A., Viti, C., & Marone, C. (2009). Fault zone fabric and fault weakness. *Nature*, *462*(7275), 907–910. doi: 10.1038/nature08585

De Paola, N., Holdsworth, R. E., Viti, C., Collettini, C., & Bullock, R. (2015). Can grain size sensitive flow lubricate faults during the initial stages of earthquake propagation? *Earth and Planetary Science Letters*, *431*, 48 - 58. doi: https://doi.org/10.1016/j.epsl.2015.09.002

Di Toro, G., Han, R., Hirose, T., De Paola, N., Nielsen, S., Mizoguchi, K., ... Shimamoto, T. (2011, mar). Fault lubrication during earthquakes. *Nature*, *471*, 494.

Dieterich, J. H. (1979). Modeling of rock friction 1. experimental results and constitutive equations. *Journal of Geophysical Research*, *84*(B5), 2161-2168.

Dieterich, J. H., & Kilgore, B. D. (1994). Direct observation of frictional contacts: New insights for state-dependent properties. *Pure and Applied Geophysics*, *143*, 283?302. doi: 10.1007/BF00874332

Dunham, E. M., Belanger, D., Cong, L., & Kozdon, J. E. (2011, 10). Earthquake Ruptures with Strongly Rate-Weakening Friction and Off-Fault Plasticity, Part1: Planar Faults. *Bulletin of the Seismological Society of America*, *101*(5), 2296-2307. doi: 10.1785/0120100075

Fang, Z., & Dunham, E. M. (2013). Additional shear resistance from fault roughness and stress levels on geometrically complex faults. *Journal of Geophysical Research: Solid Earth*, *118*(7), 3642-3654. doi: 10.1002/jgrb.50262

Faulkner, D. R., Mitchell, T. M., Behnsen, J., Hirose, T., & Shimamoto, T. (2011). Stuck in the mud? earthquake nucleation and propagation through accretionary forearcs. *Geophysical Research Letters*, *38*(18). doi: https://doi.org/

10.1029/2011GL048552

Faulkner, D. R., Mitchell, T. M., Healy, D., & Heap, M. J. (2006). Slip on 'weak' faults by the rotation of regional stress in the fracture damage zone. *Nature*, *444*(7121), 922–925. doi: 10.1038/nature05353

Field, E., Biasi, G., Bird, P., Dawson, T., Felzer, K.R., ... Zeng, Y. (2013). Uniform California Earthquake Rupture Forecast, version 3 (UCERF3) −the time-independent model. *U.S. Geological Survey Open-File Report 2013?1165, 97 p., California Geological Survey Special Report 228*. doi: http://pubs.usgs.gov/of/2013/1165/

Field, E. H., Jordan, T. H., Page, M. T., Milner, K. R., Shaw, B. E., Dawson, T. E., ... Thatcher, W. R. (2017). A synoptic view of the third Uniform California Earthquake Rupture Forecast (UCERF3). *Seismological Research Letters*, *88*(5), 1259-1267. doi: 10.1785/0220170045

Fineberg, J., & Bouchbinder, E. (2015). Recent developments in dynamic fracture: some perspectives. *International Journal of Fracture*, *196*(1), 33–57. Retrieved from `https://doi.org/10.1007/s10704-015-0038-x` doi: 10.1007/s10704-015-0038-x

Freund, L. B. (1990). *Dynamic fracture mechanics.* Cambridge University Press. doi: 10.1017/CBO9780511546761

Fukuyama, E., & Mizoguchi, K. (2010). Constitutive parameters for earthquake rupture dynamics based on high-velocity friction tests with variable sliprate. *International Journal of Fracture*, *163*(1), 15–26. doi: 10.1007/s10704-009-9417-5

Fulton, P. M., Brodsky, E. E., Kano, Y., Mori, J., Chester, F., Ishikawa, T., ... Toczko, S. a. (2013). Low coseismic friction on the Tohoku-Oki fault determined from temperature measurements. *Science*, *342*(6163), 1214–1217. doi: 10.1126/science.1243641

Gabriel, A.-A., Ampuero, J.-P., Dalguer, L. A., & Mai, P. M. (2012). The transition of dynamic rupture styles in elastic media under velocity-weakening friction. *Journal of Geophysical Research: Solid Earth*, *117*(B9). doi: 10.1029/2012JB009468

Gao, X., & Wang, K. (2014). Strength of stick-slip and creeping subduction megathrusts from heat flow observations. *Science*, *345*(6200), 1038–1041. doi: 10.1126/science.1255487

Goldsby, D. L., & Tullis, T. E. (2011). Flash heating leads to low frictional strength of crustal rocks at earthquake slip rates. *Science*, *334*(6053), 216–218. doi: 10.1126/science.1207902

Greer, J. R., Oliver, W. C., & Nix, W. D. (2005). Size dependence of mechanical properties of gold at the micron scale in the absence of strain gradients. *Acta Materialia*, *53*(6), 1821 - 1830. doi: https://doi.org/10.1016/j.actamat.2004.12.031

Gu, J.-C., Rice, J. R., Ruina, A. L., & Tse, S. T. (1984). Slip motion and stability of a single degree of freedom elastic system with rate and state dependent friction. *Journal of the Mechanics and Physics of Solids*, *32*(3), 167 - 196. doi: https://doi.org/10.1016/0022-5096(84)90007-3

Han, R., Shimamoto, T., Ando, J.-i., & Ree, J.-H. (2007). Seismic slip record in carbonate-bearing fault zones: An insight from high-velocity friction experiments on siderite gouge. *Geology*, *35*(12), 1131-1134.

Hardebeck, J. L. (2015). Stress orientations in subduction zones and the strength of subduction megathrust faults. *Science*, *349*(6253), 1213–1216. doi: 10.1126/science.aac5625

Hardebeck, J. L., & Hauksson, E. (1999). Role of fluids in faulting inferred from stress field signatures. *Science*, *285*(5425), 236–239. doi: 10.1126/science.285.5425.236

Hardebeck, J. L., & Hauksson, E. (2001). Crustal stress field in southern california and its implications for fault mechanics. *Journal of Geophysical Re-*

search: Solid Earth, *106*(B10), 21859-21882. doi: https://doi.org/10.1029/2001JB000292

Hauksson, E., Yang, W., & Shearer, P. M. (2012). Waveform Relocated Earthquake Catalog for Southern California (1981 to June 2011). *Bulletin of the Seismological Society of America*, *102*(5), 2239-2244. doi: 10.1785/0120120010

Heaton, T. H. (1990). Evidence for and implications of self-healing pulses of slip in earthquake rupture. *Physics of the Earth and Planetary Interiors*, *64*(1), 1-20.

Henyey, T. L., & Wasserburg, G. J. (1971). Heat flow near major strike-slip faults in California. *Journal of Geophysical Research (1896-1977)*, *76*(32), 7924-7946. doi: 10.1029/JB076i032p07924

Ikari, M. J., Marone, C., & Saffer, D. M. (2011, 01). On the relation between fault strength and frictional stability. *Geology*, *39*(1), 83-86. doi: 10.1130/G31416.1

Ishibe, T., & Shimazaki, K. (2012). Characteristic Earthquake Model and Seismicity around Late Quaternary Archive Faults in Japan. *Bulletin of the Seismological Society of America*, *102*(3), 1041-1058. doi: 10.1785/0120100250

Jaeger, J., & Cook, N. (1976). *Fundamentals of rock mechanics.* London: Chapman and Hall.

Jiang, J., & Lapusta, N. (2016). Deeper penetration of large earthquakes on seismically quiescent faults. *Science*, *352*(6291), 1293–1297. doi: 10.1126/science.aaf1496

Kagan, Y. Y., Jackson, D. D., & Geller, R. J. (2012). Characteristic Earthquake Model, 1884−2011, RIP. *Seismological Research Letters*, *83*(6), 951-953. doi: 10.1785/0220120107

Kaneko, Y., & Lapusta, N. (2008). Variability of earthquake nucleation in continuum models of rate-and-state faults and implications for aftershock rates. *Journal of Geophysical Research*, *113*, B12312. doi: 10.1029/2007JB005154

Lachenbruch, A. H., & Sass, J. H. (1980). Heat flow and energetics of the San Andreas Fault Zone. *Journal of Geophysical Research: Solid Earth*, *85*(B11), 6185-6222. doi: 10.1029/JB085iB11p06185

Lambert, V., & Lapusta, N. (2020). Rupture-dependent breakdown energy in fault models with thermo-hydro-mechanical processes. *Solid Earth*, *11*(6), 2283–2302. doi: 10.5194/se-11-2283-2020

Lambert, V., Lapusta, N., & Perry, S. (in press). Propagation of large earthquakes as self-healing pulses and mild cracks. *Nature*.

Lapusta, N., Rice, J. R., Ben-Zion, Y., & Zheng, G. (2000). Elastodynamic analysis for slow tectonic loading with spontaneous rupture episodes on faults with rate- and state- dependent friction. *Journal of Geophysical Research*, *105*, 765-789. doi: 10.1029/2000JB900250

Lockner, D. A., Morrow, C., Moore, D., & Hickman, S. (2011). Low strength of deep San Andreas fault gouge from SAFOD core. *Nature*, *472*(7341), 82–85. doi: 10.1038/nature09927

Lu, X., Rosakis, A. J., & Lapusta, N. (2010). Rupture modes in laboratory earthquakes: Effect of fault prestress and nucleation conditions. *Journal of Geophysical Research: Solid Earth*, *115*(B12). doi: 10.1029/2009JB006833

Marone, C. (1998). Laboratory-derived friction laws and their application to seismic faulting. *Annual Review of Earth and Planetary Sciences*, *26*(1), 643-696. doi: 10.1146/annurev.earth.26.1.643

McLaskey, G. C., Kilgore, B. D., Lockner, D. A., & Beeler, N. M. (2014). Laboratory generated m -6 earthquakes. *Pure and Applied Geophysics*, *171*(10), 2601–2615. doi: 10.1007/s00024-013-0772-9

Michailos, K., Smith, E. G., Chamberlain, C. J., Savage, M. K., & Townend, J. (2019). Variations in seismogenic thickness along the Central Alpine Fault, New Zealand, revealed by a decade's relocated microseismicity. *Geochemistry, Geophysics, Geosystems*, *20*(1), 470-486. doi: 10.1029/2018GC007743

Michel, S., Avouac, J.-P., Lapusta, N., & Jiang, J. (2017). Pulse-like partial ruptures and high-frequency radiation at creeping-locked transition during megathrust earthquakes. *Geophysical Research Letters*, *44*(16), 8345-8351. doi: 10.1002/2017GL074725

Nankali, H. R. (2011). Slip rate of the Kazerun Fault and Main Recent Fault (Zagros, Iran) from 3D mechanical modeling. *Journal of Asian Earth Sciences*, *41*, 89-98. doi: 10.1016/j.jseaes.2010.12.009

Nielsen, S., Spagnuolo, E., Violay, M., Smith, S., Di Toro, G., & Bistacchi, A. (2016). G: Fracture energy, friction and dissipation in earthquakes. *Journal of Seismology*, *20*(4), 1187–1205. doi: 10.1007/s10950-016-9560-1

Noda, H., Dunham, E. M., & Rice, J. R. (2009). Earthquake ruptures with thermal weakening and the operation of major faults at low overall stress levels. *Journal of Geophysical Research: Solid Earth*, *114*(B7). doi: 10.1029/2008JB006143

Noda, H., & Lapusta, N. (2010). Three-dimensional earthquake sequence simulations with evolving temperature and pore pressure due to shear heating: Effect of heterogeneous hydraulic diffusivity. *Journal of Geophysical Research*, *115*, B123414. doi: 10.1029/2010JB007780

Noda, H., & Lapusta, N. (2012). On averaging interface response during dynamic rupture and energy partitioning diagrams for earthquakes. *Journal of Applied Mechanics*, *79*. doi: 10.1115/1.4005964

Noda, H., Lapusta, N., & Kanamori, H. (2013). Comparison of average stress drop measures for ruptures with heterogeneous stress change and implications for earthquake physics. *Geophysical Journal International*. doi: 10.1093/gji/ggt074

Page, M. T., & Felzer, K. (2015). Southern San Andreas Fault seismicity is consistent with the Gutenberg-Richter magnitude-frequency distribution. *Bulletin of the Seismological Society of America*, *105*(4), 2070-2080. doi:

10.1785/0120140340

Page, M. T., & van der Elst, N. J. (2018). Fault-tolerant b-values and aftershock productivity. *Journal of Geophysical Research: Solid Earth*, *123*(12), 10,880-10,888. doi: https://doi.org/10.1029/2018JB016445

Perry, S. M., Lambert, V., & Lapusta, N. (2020). Nearly magnitude-invariant stress drops in simulated crack-like earthquake sequences on rate-and-state faults with thermal pressurization of pore fluids. *Journal of Geophysical Research: Solid Earth*. doi: 10.1029/2019JB018597

Pharr, G. M., Herbert, E. G., & Gao, Y. (2010). The indentation size effect: A critical examination of experimental observations and mechanistic interpretations. *Annual Review of Materials Research*, *40*(1), 271-292. doi: 10.1146/annurev-matsci-070909-104456

Rice, J. R. (2006). Heating and weakening of faults during earthquake slip. *Journal of Geophysical Research*, *111*, B05311. doi: 10.1029/2005JB004006

Rice, J. R., & Ruina, A. L. (1983). Stability of steady frictional slipping. *Journal of Applied Mechanics*, *50*(2), 343-349.

Rubin, A., & Ampuero, J.-P. (2005). Earthquake nucleation on (aging) rate and state faults. *Journal of Geophysical Research: Solid Earth*, *110*(B11).

Rubino, V., Rosakis, A. J., & Lapusta, N. (2017). Understanding dynamic friction through spontaneously evolving laboratory earthquakes. *Nature Communications*, *8*(1), 15991. doi: 10.1038/ncomms15991

Rubinstein, S. M., Cohen, G., & Fineberg, J. (2004). Detachment fronts and the onset of dynamic friction. *Nature*, *430*(7003), 1005–1009. doi: 10.1038/nature02830

Rubinstein, S. M., Cohen, G., & Fineberg, J. (2006, Jun). Contact area measurements reveal loading-history dependence of static friction. *Phys. Rev. Lett.*, *96*, 256103. doi: 10.1103/PhysRevLett.96.256103

Ruina, A. (1983). Slip instability and state variable friction laws. *Journal of Geo-*

physical Research, *88*(B12), 10359-10370.

Schwartz, D. P., & Coppersmith, K. J. (1984). Fault behavior and characteristic earthquakes– examples from the wasatch and san andreas fault zones. *Journal of Geophysical Research*, *89*, 5681-5698.

Segall, P., & Rice, J. R. (2006). Does shear heating of pore fluid contribute to earthquake nucleation? *Journal of Geophysical Research: Solid Earth*, *111*(B9). doi: 10.1029/2005JB004129

Sibson, R. H. (1973). Interactions between temperature and pore-fluid pressure during earthquake faulting and a mechanism for partial or total stress relief. *Nature*, *243*(126), 66-68.

Sibson, R. H. (1975). Generation of pseudotachylyte by ancient seismic faulting. *Geophysical Journal of the Royal Astronomical Society*, *43*(3), 775-794. doi: 10.1111/j.1365-246X.1975.tb06195.x

Sieh, K. E. (1978, 12). Central California foreshocks of the great 1857 earthquake. *Bulletin of the Seismological Society of America*, *68*(6), 1731-1749.

Simons, M., Minson, S. E., Sladen, A., Ortega, F., Jiang, J., Owen, S. E., . . . Webb, F. H. (2011). The 2011 magnitude 9.0 tohoku-oki earthquake: Mosaicking the megathrust from seconds to centuries. *Science*, *332*(6036), 1421–1425. doi: 10.1126/science.1206731

Sone, H., & Shimamoto, T. (2009). Frictional resistance of faults during accelerating and decelerating earthquake slip. *Nature Geoscience*, *2*(10), 705–708. doi: 10.1038/ngeo637

Suppe, J. (2007, 12). Absolute fault and crustal strength from wedge tapers. *Geology*, *35*(12), 1127-1130. doi: 10.1130/G24053A.1

Svetlizky, I., & Fineberg, J. (2014). Classical shear cracks drive the onset of dry frictional motion. *Nature*, *509*(7499), 205–208. doi: 10.1038/nature13202

Tanikawa, W., & Shimamoto, T. (2009). Frictional and transport properties of the chelungpu fault from shallow borehole data and their correlation with seismic behavior during the 1999 Chi-Chi earthquake. *Journal of Geophysical Research: Solid Earth*, *114*(B1). doi: 10.1029/2008JB005750

Tenthorey, E., & Cox, S. F. (2006). Cohesive strengthening of fault zones during the interseismic period: An experimental study. *Journal of Geophysical Research: Solid Earth*, *111*(B9). doi: https://doi.org/10.1029/2005JB004122

Thom, C. A., Brodsky, E. E., Carpick, R. W., Pharr, G. M., Oliver, W. C., & Goldsby, D. L. (2017). Nanoscale roughness of natural fault surfaces controlled by scale-dependent yield strength. *Geophysical Research Letters*, *44*(18), 9299-9307. doi: 10.1002/2017GL074663

Tinti, E., Fukuyama, E., Piatanesi, A., & Cocco, M. (2005). A Kinematic Source-Time Function Compatible with Earthquake Dynamics. *Bulletin of the Seismological Society of America*, *95*(4), 1211-1223. doi: 10.1785/0120040177

Tinti, E., Scognamiglio, L., Michelini, A., & Cocco, M. (2016). Slip heterogeneity and directivity of the ML 6.0, 2016, Amatrice earthquake estimated with rapid finite-fault inversion. *Geophysical Research Letters*, *43*(20).

Tormann, T., Wiemer, S., & Mignan, A. (2014). Systematic survey of high-resolution b value imaging along californian faults: Inference on asperities. *Journal of Geophysical Research: Solid Earth*, *119*(3), 2029-2054. doi: https://doi.org/10.1002/2013JB010867

Townend, J., & Zoback, M. D. (2000). How faulting keeps the crust strong. *Geology*, *28*(5), 399-402. doi: 10.1130/0091-7613(2000)28⟨399:HFKTCS⟩2.0.CO;2

Townend, J., & Zoback, M. D. (2004). Regional tectonic stress near the San Andreas fault in central and Southern California. *Geophysical Research Letters*, *31*(15). doi: 10.1029/2003GL018918

Tsutsumi, A., & Shimamoto, T. (1997). High-velocity frictional properties of gabbro. *Geophysical Research Letters*, *24*(6), 699-702. doi: 10.1029/97GL00503

Uchic, M. D., Dimiduk, D. M., Florando, J. N., & Nix, W. D. (2004). Sample dimensions influence strength and crystal plasticity. *Science*, *305*(5686), 986–

989. doi: 10.1126/science.1098993

Wesnousky, S. G. (1994). The Gutenberg-Richter or characteristic earthquake distribution, which is it? *Bulletin of the Seismological Society of America*, *84*(6), 1940-1959.

Wibberley, C. A. J., Yielding, G., & Toro, G. D. (2008). Recent advances in the understanding of fault zone internal structure: a review. In *The Internal Structure of Fault Zones: Implications for Mechanical and Fluid-Flow Properties.* Geological Society of London. doi: 10.1144/SP299.2

Yamashita, F., Fukuyama, E., Mizoguchi, K., Takizawa, S., Xu, S., & Kawakata, H. (2015). Scale dependence of rock friction at high work rate. *Nature*, *528*(7581), 254–257. doi: 10.1038/nature16138

Yasuhara, H., Marone, C., & Elsworth, D. (2005). Fault zone restrengthening and frictional healing: The role of pressure solution. *Journal of Geophysical Research: Solid Earth*, *110*(B6). doi: https://doi.org/10.1029/2004JB003327

Ye, L., Lay, T., Kanamori, H., & Rivera, L. (2016a). Rupture characteristics of major and great (Mw > 7.0) megathrust earthquakes from 1990 to 2015: 1. source parameter scaling relationships. *Journal of Geophysical Research: Solid Earth*, *121*(2), 826-844. doi: 10.1002/2015JB012426

Ye, L., Lay, T., Kanamori, H., & Rivera, L. (2016b). Rupture characteristics of major and great (Mw > 7.0) megathrust earthquakes from 1990 to 2015: 2. depth dependence. *Journal of Geophysical Research: Solid Earth*, *121*(2), 845-863. doi: 10.1002/2015JB012427

Zheng, G., & Rice, J. R. (1998). Conditions under which velocity-weakening friction allows a self-healing versus a crack-like mode of rupture. *Bulletin of the Seismological Society of America*, *88*(6), 1466-1483.

Zoback, M., Hickman, S., & Ellsworth, W. (2010). Scientific drilling into the San Andreas fault zone. *Eos, Transactions American Geophysical Union*, *91*, 197-199. doi: 10.1029/2010EO220001

Supporting Information for "Scale dependence of earthquake rupture prestress in models with enhanced weakening: implications for event statistics and inferences of fault stress"

Valère Lambert[1] Nadia Lapusta[1,2] Daniel Faulkner[3]

[1]Seismological Laboratory, California Institute of Technology, Pasadena, California, USA

[1,2]Department of Mechanical and Civil Engineering, California Institute of Technology, Pasadena, California, USA

[3]School of Environmental Sciences, University of Liverpool, Liverpool, UK

Contents of this file

S1. Methodology for simulations of sequences of earthquakes and aseismic slip with and without the thermal pressurization of pore fluids

In order to conduct numerical simulations of sequences of spontaneous earthquakes and aseismic slip, we utilize the spectral boundary integral method to solve the elastodynamic equations of motion with the friction boundary conditions, including the evolution of pore fluid pressure and temperature on the fault coupled with off-fault diffusion (Lapusta et al., 2000; Noda & Lapusta, 2010). Our fault models are governed by a form of the laboratory-derived Dieterich-Ruina rate-and-state friction law regularized for zero and negative slip rates, with the state evolution governed by the aging law (Rice & Ben-Zion, 1996; Noda & Lapusta, 2010). The most commonly used formulation of rate-and-state laws is the Dieterich-Ruina formulation (Dieterich, 1979; Ruina, 1983):

$$\tau = \overline{\sigma} f(V, \theta) = (\sigma - p) \left[f_* + a \ln \frac{V}{V_*} + b \ln \frac{\theta V_*}{L} \right], \tag{S1}$$

where f_* is a reference steady-state friction coefficient at reference sliding rate V_*, L is the characteristic slip distance, and a and b are the direct effect and evolution effect parameters, respectively. During steady-state sliding ($\dot{\theta} = 0$), the friction coefficient is expressed as:

$$f_{ss}(V) = f_* + (a - b) \ln \frac{V}{V_*}, \tag{S2}$$

where the combination of frictional properties $(a - b) > 0$ results in steady-state velocity-strengthening (VS) behavior, where stable slip is expected, and properties resulting in $(a - b) < 0$ lead to steady-state velocity-weakening (VW) behavior, where accelerating slip and hence stick-slip occur for sufficiently large regions.

The peak shear stress during dynamic rupture propagation can correspond to a much higher apparent friction coefficient than the reference friction coefficient f_* or the similar steady-state friction coefficient at seismic slip rates of the order of 1 m/s. Assuming that the fault has been locked interseismically with the state variable healing to a value θ_{int} and the slip rate rapidly accelerates to the peak slip rate V_{peak} upon arrival of the rupture front with negligible evolution of the state variable $\theta \approx \theta_{\text{int}}$, the peak friction can be approximately given as:

$$
\begin{aligned}
\tau_{\text{peak}}/(\sigma - p_{\text{int}}) &= f_* + a\ln\frac{V_{\text{peak}}}{V_*} + b\ln\frac{\theta_{\text{int}}}{\theta_{\text{ss}}(V_*)} \\
&= \frac{\tau_{\text{ss}}(V_{\text{peak}})}{(\sigma - p_{\text{int}})} + b\ln\frac{\theta_{\text{int}}}{\theta_{\text{ss}}(V_{\text{peak}})} \\
&= \frac{\tau_{\text{ss}}(V_{\text{pl}})}{(\sigma - p_{\text{int}})} + (a-b)\ln\frac{V_{\text{peak}}}{V_{\text{pl}}} + b\ln\frac{\theta_{\text{int}}}{\theta_{ss}(V_{\text{peak}})}
\end{aligned} \tag{S3}
$$

Note that $V_{\text{peak}} \gg V_* \gg V_{\text{pl}}$ and $\theta_{\text{int}} \gg \theta_{\text{ss}}(V_*) \gg \theta_{\text{ss}}(V_{\text{peak}})$ for typical seismic slip rates and interseismic durations of healing. The last two terms on the third line gives the difference between the local SSQS shear resistance described in the main text and the peak shear resistance, where the last term typically dominates for periods of extending healing and higher values of θ_{int}. Consequently, for a given dynamic slip rate V_{peak}, the better healed the interface with higher θ_{ini}, the higher the peak friction during dynamic rupture (Lambert & Lapusta, 2020).

The standard Dieterich-Ruina formulation (equation S1) has been empirically-determined from laboratory experiments at sliding rates between 10^{-9} m/s to around 10^{-3} m/s. Under the standard logarithmic formulation, friction becomes negative as the slip rate V approaches zero and is undefined for zero or negative slip rates (Figure S5). The standard formulation may be regularized near $V = 0$ such that the shear resistance remains positive for all positive values of V (Rice & Ben-Zion, 1996):

$$
\tau(V,\theta) = a\overline{\sigma}\sinh^{-1}\left[\frac{V}{2V_*}\exp\left(\frac{f_* + b\log(\theta V_*/L)}{a}\right)\right], \tag{S4}
$$

with the steady-state shear resistance given by:

$$\tau_{ss}(V) = a\overline{\sigma}\sinh^{-1}\left[\frac{V}{2V_*}\exp\left(\frac{f_* + b\log(V_*/V)}{a}\right)\right]. \tag{S5}$$

Theoretical justification for such regularization has been provided by drawing analogy between the direct velocity effect and the exponential formulation of thermally-activated creep at contact junctions, where the contact shear stress acts as a biasing factor (Rice et al., 2001). The standard logarithmic rate-dependent formulation is derived when only considering forward activated jumps, which may be dominant under significant shear stress and conditions relevant to most laboratory experiments. The regularized formulation (equation S4) arises when including the presence of backward jumps, which are equally probable as forward jumps for $\tau = 0$, as in the full thermally-activated creep theory. The logarithmic and regularized formulations are equivalent for conditions consistent with laboratory experiments, and differ only for very low slip rates (Figure S5).

Earthquakes may nucleate only if the VW region is larger than the nucleation size h^*. For 2D problems, two theoretical estimates of the nucleation size in mode III are (Rice & Ruina, 1983; Rubin & Ampuero, 2005):

$$h^*_{RR} = \frac{\pi}{4}\frac{\mu L}{(b-a)(\sigma - p)};\ h^*_{RA} = \frac{2}{\pi}\frac{\mu L b}{(b-a)^2(\sigma - p)}, \tag{S6}$$

where μ is the shear modulus. The simulated fault in our models contains a 24-km region with VW frictional properties surrounded by VS regions to create a 72-km frictional region. Outside of this frictional regions, the fault moves with a prescribed plate rate V_{pl} to provide tectonic-like loading (Figure 2A of main text).

The thermal pressurization of pore fluids is governed in our simulations by the following coupled differential equations for temperature and pore pressure evolution (Noda & Lapusta, 2010):

$$\frac{\partial T(y,z;t)}{\partial t} = \alpha_{\mathrm{th}} \frac{\partial^2 T(y,z;t)}{\partial y^2} + \frac{\tau(z;t)V(z;t)}{\rho c} \frac{\exp(-y^2/2w^2)}{\sqrt{2\pi} w}, \tag{S7}$$

$$\frac{\partial p(y,z;t)}{\partial t} = \alpha_{\mathrm{hy}} \frac{\partial^2 p(y,z;t)}{\partial y^2} + \Lambda \frac{\partial T(y,z;t)}{\partial t}, \tag{S8}$$

where T is the temperature of the pore fluid, α_{th} is the thermal diffusivity, τV is the shear heating source distributed over a Gaussian shear layer of half-width w, ρc is the specific heat, y is the distance normal to the fault plane, α_{hy} is the hydraulic diffusivity, and Λ is the coupling coefficient that gives pore pressure change per unit temperature change under undrained conditions. To approximate the effects of off-fault yielding we employ a velocity limit of $V_{\mathrm{max}} = 15$ m/s, as discussed in detail in Lambert et al. (in press). This approximation is motivated by detailed dynamic rupture simulations with off-fault yielding (Andrews, 2004), with the value of velocity limited corresponding to a representative seismogenic depth of 10 km.

Our simulations include fault models with varying levels of ambient fluid overpressure in terms of effective normal stress and as well as degrees of efficiency due to enhanced weakening due to thermal pressurization. Parameters for the simulations are given in Tables 1-3. Note that the stress changes associated with standard rate-and-state friction have a relatively mild logarithmic dependence on slip rate and are directly proportional to the effective confining stress. As such, persistently weak rate-and-state fault models with low effective normal stress and no enhanced weakening result in generally mild static stress drops (≤ 2 MPa) for typical frictional parameters measured in the laboratory (Figure 2 of main text). Thus, the inclusion of at least mild enhanced dynamic weakening is required for fault models with low effective normal stress, such as due to substantial fluid overpressurization, to produce average static stress drops between 1 - 10 MPa, as typically inferred for natural earthquakes (Figures 11 of main text and S3; Lambert et al., in press).

In order to examine the prestress at the beginning of dynamic ruptures, we define the beginning and end of dynamic rupture, as well as the ruptured area, based on a slip velocity threshold ($V_{\text{thresh}} = 1$ cm/s) for seismic slip. We have found in previous studies that varying V_{thresh} between by 10^{-3} to 10^{-1} m/s results in minor variations of the determined rupture timing and area, within 1% (Perry et al., 2020; Lambert et al., in press).

Our fault models with more efficient enhanced dynamic weakening produce fewer smaller events than those with mild to moderate enhanced weakening, as can be observed in the frequency-magnitude statistics (Figure 10 of the main text). To create frequency-magnitude histograms we compute the seismic moment $M_0 = \mu A \overline{\delta}$ for ruptures, where μ is the shear modulus, A is the rupture area and $\overline{\delta}$ is the average slip in the rupture. As our simulations are 2-D, we compute the moment by assuming a circular rupture area $A = \pi(\lambda_{\text{rupt}}/2)^2$, where λ_{rupt} is the rupture length.

S2. Single-degree-of-freedom representation of laboratory experiments

We compare the evolution of local slip rate and shear stress in our simulated dynamic ruptures with single-degree-of-freedom (SDOF) calculations motivated by high-velocity laboratory experiments that impose variable seismic slip rates to infer shear resistance evolution and often compare their findings with seismological observations (Sone & Shimamoto, 2009; Fukuyama & Mizoguchi, 2010). The SDOF calculations are governed by the same rate-and-state friction with enhanced dynamic weakening due to thermal pressurization as in our fault model TP4. Our SDOF calculations impose a slip-rate history, as typically done in laboratory experiments, and solve for the evolution of shear stress, state variable, temperature and pore pressure using equation 3 of the main text and equations S4 and S7-8 given the initial state. We assume initial conditions where sliding has been maintained until steady-state conditions at the slip rate of $V = 0.1$ mm/s, comparable to the initial conditions of Fukuyama and Mizoguchi (2010). We then impose two different slip rate functions characterized by regularized Yoffe functions (Tinti et al., 2005), with total slip of 1.95 m (comparable to our simulated slip) and maximum slip rate of 2 m/s. Tinti et al. (2005) regularized the stress singularity in the analytical Yoffe function by convolving it with a triangular function of half-width t_s. The regularized Yoffe functions are characterized by two time-scales, the half-width t_s and the rise time t_r. For the two examples shown in Figure 9 of the main text, we choose values of $t_r = 3$s with $t_s = 0.1t_r$ for RYF1 and $t_r = 1.4$s with $t_s = 0.4t_r$ for RYF2, in order to compare pulses with more pronounced and gradual accelerations that produce the same slip and peak slip rate.

References

Andrews, D. J. (2004, 06). Rupture Models with Dynamically Determined Breakdown Displacement. *Bulletin of the Seismological Society of America*, *94*(3), 769-775. doi: 10.1785/0120030142

Dieterich, J. H. (1979). Modeling of rock friction 1. experimental results and constitutive equations. *Journal of Geophysical Research*, *84*(B5), 2161-2168.

Fukuyama, E., & Mizoguchi, K. (2010). Constitutive parameters for earthquake rupture dynamics based on high-velocity friction tests with variable sliprate. *International Journal of Fracture*, *163*(1), 15–26. doi: 10.1007/s10704-009-9417-5

Lambert, V., & Lapusta, N. (2020). Rupture-dependent breakdown energy in fault models with thermo-hydro-mechanical processes. *Solid Earth*, *11*(6), 2283–2302. doi: 10.5194/se-11-2283-2020

Lambert, V., Lapusta, N., & Perry, S. (in press). Propagation of large earthquakes as self-healing pulses and mild cracks. *Nature*.

Lapusta, N., Rice, J. R., Ben-Zion, Y., & Zheng, G. (2000). Elastodynamic analysis for slow tectonic loading with spontaneous rupture episodes on faults with rate- and state- dependent friction. *Journal of Geophysical Research*, *105*, 765-789. doi: 10.1029/2000JB900250

Noda, H., & Lapusta, N. (2010). Three-dimensional earthquake sequence simulations with evolving temperature and pore pressure due to shear heating: Effect of heterogeneous hydraulic diffusivity. *Journal of Geophysical Research*, *115*, B123414. doi: 10.1029/2010JB007780

Perry, S. M., Lambert, V., & Lapusta, N. (2020). Nearly magnitude-invariant stress drops in simulated crack-like earthquake sequences on rate-and-state faults with thermal pressurization of pore fluids. *Journal of Geophysical Research: Solid Earth*, e2019JB018597. doi: 10.1029/2019JB018597

Rice, J. R., & Ben-Zion, Y. (1996, 04). Slip complexity in earthquake fault models. *Proceedings of the National Academy of Sciences of the United States of America*, *93*(9), 3811–3818. doi: 10.1073/pnas.93.9.3811

Rice, J. R., Lapusta, N., & Ranjith, K. (2001). Rate and state dependent friction and the stability of sliding between elastically deformable solids. *Journal of the Mechanics and Physics of Solids*, *49*(9), 1865-1898.

Rice, J. R., & Ruina, A. L. (1983). Stability of steady frictional slipping. *Journal of Applied Mechanics*, *50*(2), 343-349.

Rubin, A., & Ampuero, J.-P. (2005). Earthquake nucleation on (aging) rate and state faults. *Journal of Geophysical Research: Solid Earth*, *110*(B11).

Ruina, A. (1983). Slip instability and state variable friction laws. *Journal of Geophysical Research*, *88*(B12), 10359-10370.

Sone, H., & Shimamoto, T. (2009). Frictional resistance of faults during accelerating and decelerating earthquake slip. *Nature Geoscience*, *2*(10), 705–708. doi: 10.1038/ngeo637

Tinti, E., Fukuyama, E., Piatanesi, A., & Cocco, M. (2005). A Kinematic Source-Time Function Compatible with Earthquake Dynamics. *Bulletin of the Seismological Society of America*, *95*(4), 1211-1223. doi: 10.1785/0120040177

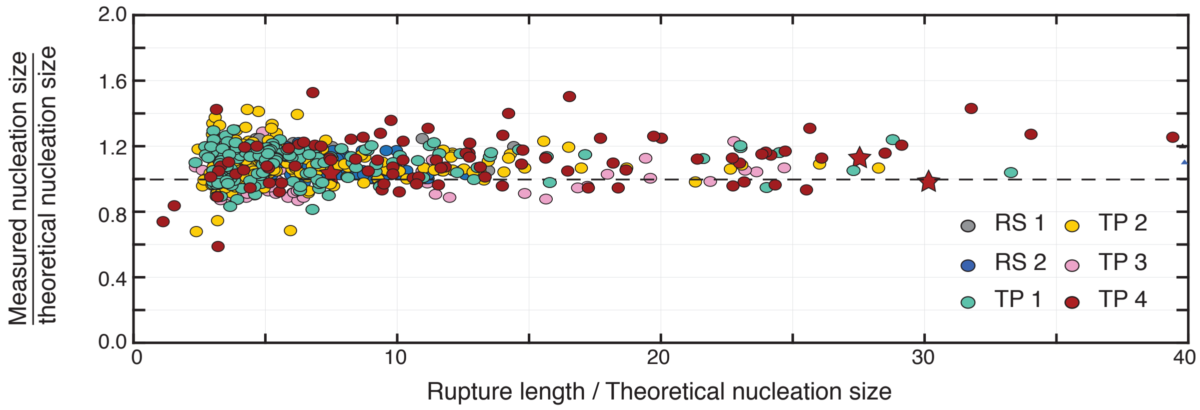

Figure S1. The measured nucleation sizes of the simulated ruptures are comparable to the theoretical estimate h^*_{RA}, within a factor of 2.

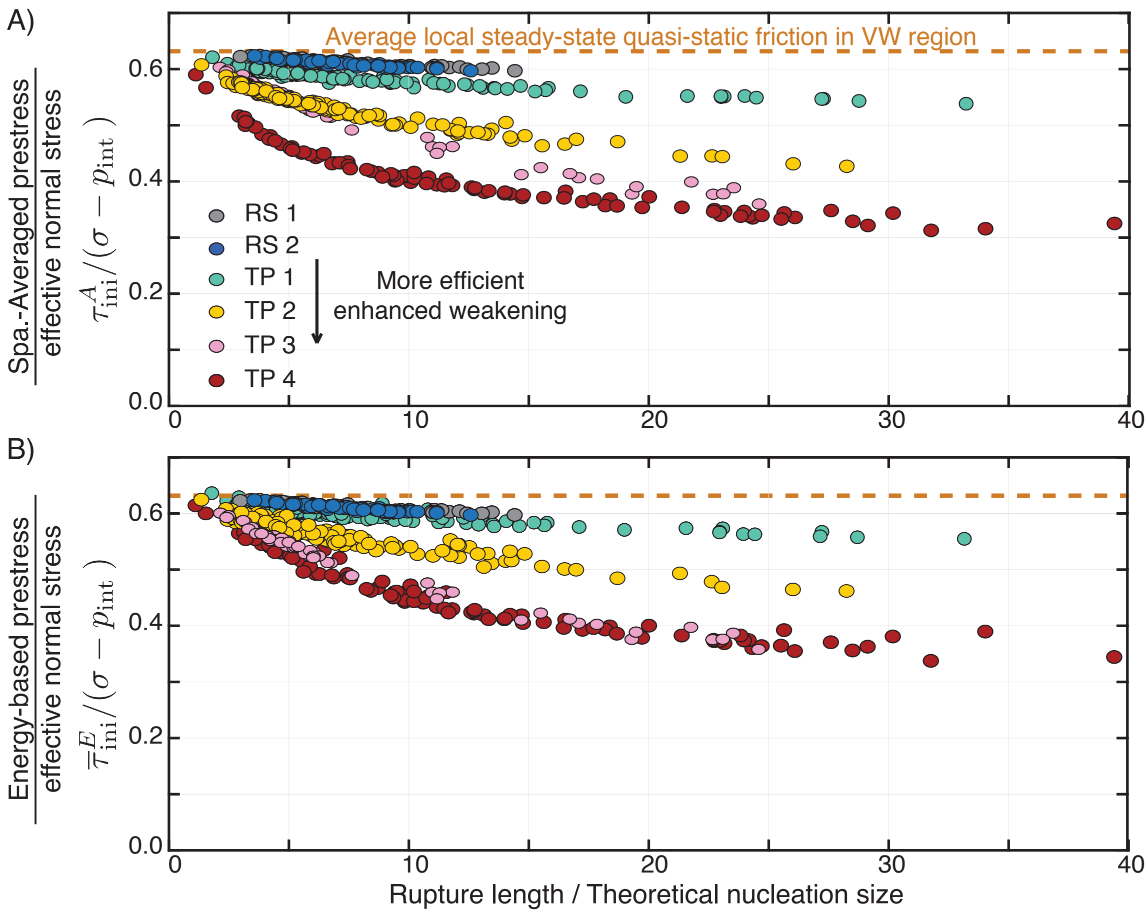

Figure S2. The spatially-averaged prestress τ_{ini}^{A} and energy-averaged prestress $\overline{\tau}_{\mathrm{ini}}^{E}$ are generally comparable and decrease with increasing rupture size and efficiency of weakening.

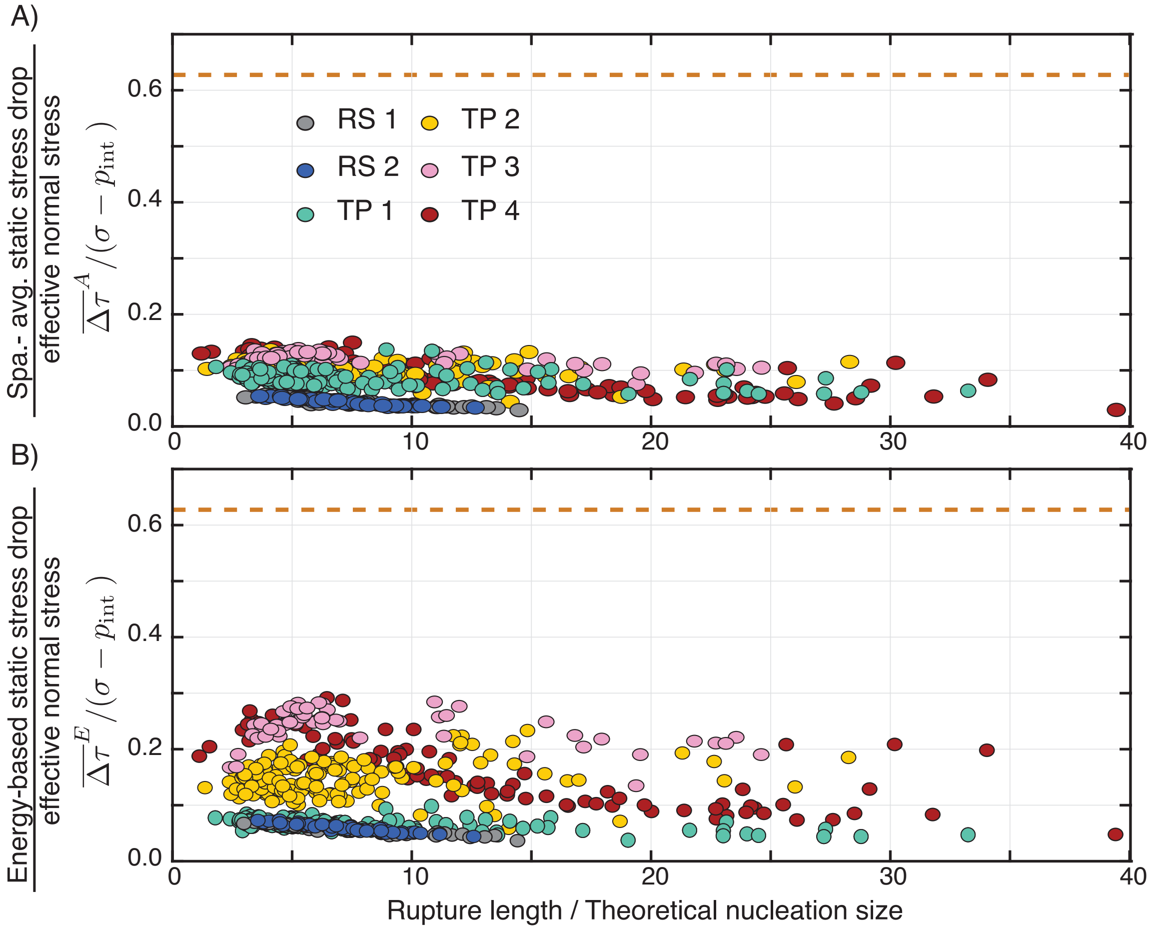

Figure S3. The (A) spatially-averaged and (B) energy-based average static stress drops for ruptures represent relatively mild decreases in average shear stress with respect to the effective normal stress. Persistently weak fault models with low effective normal stress $\leq$ 20 MPa and relatively mild weakening, such as from standard rate-and-state friction (RS1 and RS2) produce potentially too small average static stress drops $\leq$ 2 MPa, whereas models with mild to moderate enhanced weakening (TP1-4) produce realistic average static stress drops of 1 - 10 MPa.

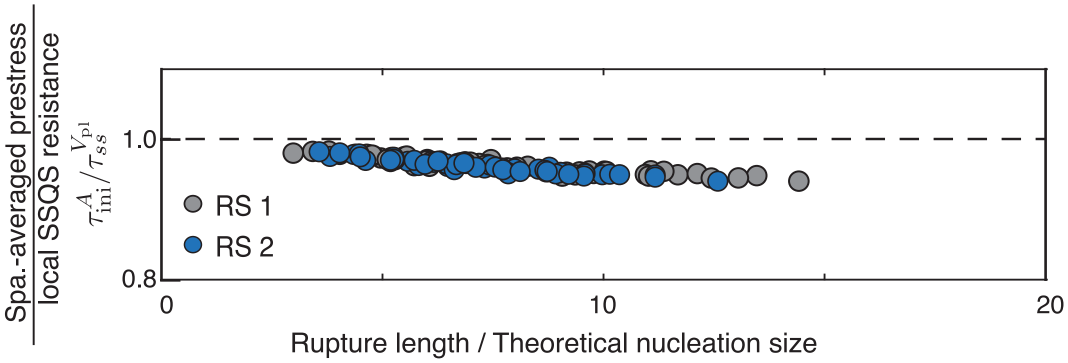

Figure S4. Ruptures on fault models with relatively mild weakening due to standard rate-and-state friction also exhibit a mild decrease in the spatially-averaged prestress τ_{ini}^{A} with increasing rupture size.

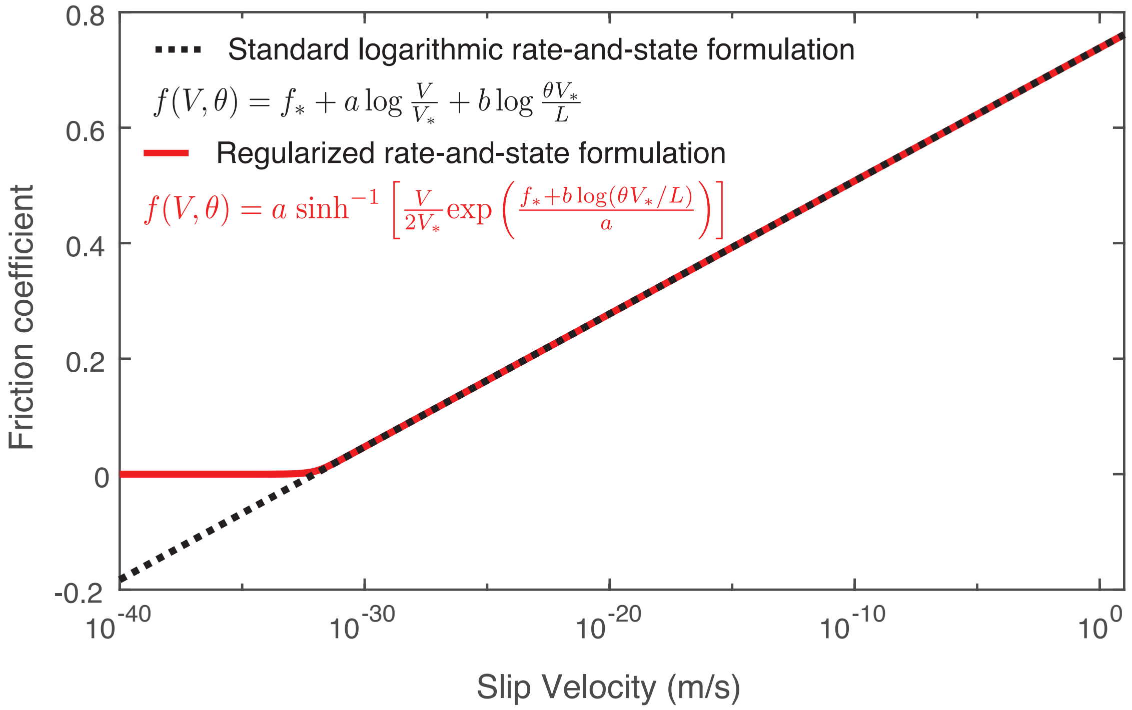

Figure S5. Comparison of the standard logarithmic (black) and regularized (red) formulations for rate-and-state friction given fixed $\theta = L/V_*$ with $V_* = 1$ μm/s, $f_* = 0.6$, and $(a - b) = 0.004$. The two formulations are equivalent for slip rates relevant to most laboratory experiments but differ as V approaches 0 m/s.